Interactions between multiple physical particle injection pumps in the Southern Ocean

Andrew F. Thompson[1], Lilian A. Dove[1], Ellie Flint[1,2], Leo Lacour[3,4], Philip Boyd[3]

[1]Environmental Science and Engineering, California Institute of Technology, Pasadena, CA, USA
[2]University of California, San Diego, La Jolla, CA, USA
[3]Institute for Marine and Antarctic Studies, University of Tasmania, Hobart, Australia
[4]Sorbonne Université, CNRS, Laboratoire d'Océanographie de Villefranche, Villefranche sur Mer, France

Key Points:

- Observations from a quasi-Lagrangian float and ocean glider provide insight into physical contributions to the biological pump.
- Regimes are identified when mixed layer and eddy subduction pumps are in opposition and work in tandem.
- The vertical structure of eddy stirring and transport by submesoscale motions strongly influences the coupling of various biological pumps.

Corresponding author: Andrew Thompson, `andrewt@caltech.edu`

Abstract

The biological pump, which removes carbon from the surface ocean and regulates atmospheric carbon dioxide, comprises multiple processes that include but extend beyond gravitational settling of organic particles. Contributions to the biological pump that arise from the physical circulation are broadly referred to as physical particle injection pumps; a synthetic view of how these physical pumps interact with each other and other components of the biological pump does not yet exist. In this study, observations from a quasi-Lagrangian float and ocean glider, deployed in the Southern Ocean's subantarctic zone for one month during the spring bloom, offer insight into daily-to-monthly fluctuations in the mixed layer pump and the eddy subduction pump. Estimated independently, each mechanism contributes intermittent export fluxes on the order of several hundreds milligrams of particulate organic carbon (POC) per day. The float and the glider produce similar estimates of the mixed layer pump, with sustained weekly periods of export fluxes with a magnitude of $\sim$400 mg POC m^{-2} day^{-1}. Export fluxes from the eddy subduction pump, based on a mixed layer instability scaling, occasionally exceed 500 mg POC m^{-2} day^{-1}, with some periods having strong inferred vertical velocities and others having enhanced isopycnal slopes. Regimes occur when a summation of the two pump estimates may misrepresent the total physical carbon flux. Disentangling contributions from different physical pump mechanisms from sparse data will remain challenging. Insight into how mesoscale stirring and submesocale velocities set the vertical structure of POC concentrations is identified as a key target to reduce uncertainty in global carbon export fluxes.

Plain Language Summary

The ocean influences the global carbon cycle by transferring carbon from the surface into the deep ocean, where it is sequestered from exchange with the atmosphere for periods of decades to millennia. Marine organisms enhance this downward transfer by fixing dissolved CO2 into organic matter during photosynthesis (at the ocean surface) and removing the carbon through sinking of organic matter or via consumption and defecation by higher trophic levels. These processes are collectively referred to as the biological pump. Processes controlled by the ocean circulation, termed "physical" processes, can also influence the vertical transfer of fixed carbon to the ocean interior. Various proposed physical carbon pump mechanisms have been assessed independently without considering potential interactions between them. Here, we use data sets collected from different autonomous vehicles deployed in the Southern Ocean to provide a first look at interactions between two physical carbon pumps: the mixed layer and eddy subduction pumps. These pumps make a significant contribution to total carbon export, but there are times when they work in tandem and times when they work in opposition. The vertical structure of particulate organic carbon is identified as a key target for future observations to better constrain the biological pump.

1 Introduction: Physically-induced particle pumps as a component of the biological pump

A small fraction of the ocean's volume, limited to the well-mixed ocean surface boundary layer, or the mixed layer, directly exchanges carbon dioxide (CO_2) with the atmosphere. Any process that transports carbon, in particulate or dissolved form, across the base of the mixed layer removes it from further exchange with the atmosphere for timescales spanning months to millenia. This timescale is primarily determined by the penetration depth of the carbon export before remineralization occurs (Yamanaka & Tajika, 1996; Kwon et al., 2009). The ocean's large scale, overturning circulation is associated with the solubility pump, in which cold waters, rich in dissolved inorganic carbon (DIC) are preferentially carried to depth in polar regions and exported to lower latitudes (Sarmiento & Gruber, 2006). In contrast, biological processes that fix carbon as organic matter in the surface ocean and export the carbon as particulate organic carbon (POC) via gravitational sinking, the biological gravitational pump (BGP), is a global process (Siegel et al., 2023). Observations collected over the past decade provide convincing evidence that, at least regionally, physical processes that advect and stir surface properties to depth, known as physically-induced particle injection pumps (PPIPs), make a non-negligible contribution to the biological pump (Lévy et al., 2012; Omand et al., 2015; Stukel & Ducklow, 2017; Boyd et al., 2019). Carbon export due to PPIPs depends on both ecosystem organization, *e.g.* surface chlorophyll concentration and community composition, and physical properties, *e.g.* mixed layer depth and front intensity, which vary from sub-kilometer to many tens of kilometers spatial scales (Mahadevan, 2016; Lévy et al., 2018; Taylor, 2018; Ruiz et al., 2019). PPIPs are typically more spatially heterogeneous than the BGP or the solubility pump, and quantification of carbon fluxes due to various PPIPs remains immature.

The eddy subduction pump (ESP) refers to processes that enhance vertical velocities and vertical transport of dissolved and organic carbon across the base of the mixed layer. Most of the energy in the global ocean resides in geostrophically-balanced, mesoscale flows that are predominantly horizontal. Geostrophic balance begins to break down at scales roughly smaller than 10 km, the submesoscale dynamical regime, at which vertical velocities strengthen through ageostrophic motions. A number of physical processes can elevate vertical velocities or turbulent mixing at the ocean's submesoscale as described in reviews by McWilliams (2016) and Taylor and Thompson (2023). Submesocale advective fluxes are generally localized to small-scale fronts and arise from a tendency for ageostrophic cross-frontal vertical velocities to reduce the strength of the front. Most previous studies of the submesoscale ESP have focused on the role of mixed layer baroclinic instability, in which the magnitude of vertical velocities and export fluxes can be related to observable surface properties, such as mixed layer depth (MLD) and the magnitude of horizontal density gradients in the ocean's surface boundary layer (Omand et al., 2015), with some caveats. In particular, the theory underpinning the parameterization assumes that vertical velocities peaks at the center of the mixed layer and decay to zero at the mixed layer base, implying negligible carbon export out of the mixed layer. Yet, submesocale motions may extend deeper into the water column (below the mixed layer) as the stratification at the base of the mixed layer weakens (Callies et al., 2016; Erickson & Thompson, 2018). Nevertheless, mixed layer baroclinic instability has provided a useful approach for estimating the relative importance of submesoscale vertical velocities on a global scale. Omand et al. (2015) estimate that for large swaths of the ocean, notably the North Atlantic and the Southern Ocean's Subtropical Frontal Zone, eddy subduction may account for 25%-50% of springtime carbon export.

While vertical carbon fluxes are enhanced at submesoscale fronts (Ruiz et al., 2009), mesoscale eddies contribute to the generation and distribution of these fronts, especially in areas of strong strain at eddy peripheries that support frontogenesis (Brannigan, 2016; Thomas et al., 2013; Su et al., 2020; Siegelman et al., 2020; Freilich & Mahadevan, 2021).

Mesoscale stirring properties are spatially heterogeneous in the ACC, which modifies tracer variance on isopycnal surfaces (Dove et al., 2021) and exchange between the mixed layer and ocean interior (Brady et al., 2021; Dove et al., 2022). Llort et al. (2018) found evidence of largely unmodified surface waters, identified by low apparent oxygen utilization (AOU) values, hundreds of meters below the mixed layer using biogeochemical-Argo floats. These anomalies were localized to regions of high eddy kinetic energy (EKE) found in the lee of major Southern Ocean topographic features, but were only identified in $\sim$ 1% of all profiles. Siegelman et al. (2020) used high-resolution measurements collected from an instrumented elephant seal to suggest that mesoscale frontogenesis enhances vertical velocities well below the base of the mixed layer. Finally, Siegelman et al. (2020) and Dove et al. (2022) showed the utility of the Lagrangian-based diagnostic, finite size Lypaunov exponents (FSLEs, section 2.4; d'Ovidio et al. (2004)), for mapping spatial variations in small-scale subduction in the Southern Ocean with exchange again elevated in regions of strong mesoscale strain. These studies highlight the important coupling between mesoscale and submesoscale motions; the impact of this coupling on the biological pump remains underexplored.

Mesoscale motions and coherent mesoscale eddies not only modulate the magnitude and distribution of the upper ocean submesoscale velocity field, but they also contribute to the delivery of surface tracers and particulate matter to depth. Recent studies suggest that small-scale fronts are the sites where surface properties are imprinted on density surfaces immediately below the base of the mixed layer. This establishes a concentration gradient on that isopycnal that is subsequently stirred out by mesoscale processes (Balwada et al., 2018; Ruiz et al., 2019; Freilich & Mahadevan, 2021). The edges of mesoscale eddies are consistently identified as key locations of enhanced surface-interior exchange, enhanced isopycnal tracer gradients, and intensified isopycnal tilting. Mesoscale eddies may also modify biomass and nutrient availability through Ekman pumping and isopycnal displacement, further influencing carbon export (Rohr et al., 2020a, 2020b). Finally, the influence of mesoscale motions can extend beyond passive tracers and influence biology, for example through controls on nutrient transport (Patel et al., 2020) and the structure of surface chlorophyll (Cornec et al., 2021). Of particular relevance here, Penna et al. (2022) report finescale interleaving of distinct mesopelagic micronekton communities along the periphery of a mesoscale eddy in the Southern Ocean Subantarctic Zone, close to the location of our present study.

The mixed layer pump (MLP) is a PPIP traditionally associated with one-dimensional (vertical) processes that influence the seasonal cycle of MLD. Export via the mixed layer pump over an annual timescale is associated with the accumulation of POC in the surface mixed layer during spring and summer growth seasons, a redistribution of this POC to greater depths as the mixed layer deepens in winter, and a final "export" or detrainment of carbon as the ML shoals in the spring (Gardner et al., 1995). However, the MLP may act on shorter timescales, spanning months to weeks, or even days, the latter associated with abrupt restratificaiton events caused by submesoscale mixed layer instabilities (Thompson et al., 2016). Dall'Olmo et al. (2016) combined observations from Argo floats and remote sensing data to estimate the magnitude of the seasonal MLP and found that in high-latitude regions, where large fluctuations in MLD are common over an annual cycle, up to a quarter of the carbon flux to the mesopelagic zone occurs through the MLP; in localized regions the MLP can account for 100% of the carbon export. Higher frequency sampling from ocean gliders, as compared to Argo floats, provided the opportunity to estimate daily POC flux estimates from the MLP at daily temporal resolution in the North Atlantic and revealed a qualitatively similar importance of the MLP (Bol et al., 2018). Specifically, small-particle POC transfer across the base of the mixed layer was most efficient in winter and early spring, contributing between 5% and 25% of the total export flux. Daily estimates of POC export via the MLP produced large fluxes related to both export and entrainment, with a small residual emerging at monthly timescales.

The amplitude was particularly large in the January to May time period, associated with high frequency fluctuations in the MLD at this location (Damerell et al., 2020).

The physical and biological mechanisms that carry POC across the base of the mixed layer in the Southern Ocean and modify tracer properties on interior density surfaces has an out-sized impact on the global marine carbon cycle. Tracers in the Southern Ocean undergo strong stirring due to the generally high levels of EKE while also residing in regions of relatively weak vertical surface stratification, which may precondition the biological pump to have substantial contributions to export from the ESP and the MLP (Omand et al., 2015; Gille et al., 2022; Lacour et al., 2023). Additionally, the seasonal cycle of sea ice melt induces large-scale surface density gradients cascade to smaller scales via mesoscale stirring, producing in small-scale density fronts susceptible to hydrodynamic instabilities and enhanced vertical velocities (Giddy et al., 2021, 2022). The prevalence of these submesoscale processes are not uniformly distributed over the Southern Ocean, but are concentrated in regions of high EKE downstream of major topographic features (Gille & Kelly, 1996), which are also hotspots of subduction (Dove et al., 2023). The increased deployment of biogeochemical-Argo floats, in particular through the SOCCOM project (Bushinsky et al., 2019), has improved understanding of the large-scale distribution of biogeochemical properties in the Southern Ocean, and a few studies have shown how these floats can help to capture regional and smaller-scale processes that shape these distributions (Llort et al., 2018) and their interannual variability (Lacour et al., 2023).

In this study, we provide estimates of carbon export PPIPs in the Southern Ocean using observations from two different autonomous platforms: an ocean glider and a quasi-Lagrangian float (section 2). These observations were collected as part of the SOLACE (Southern Ocean Large Areal Carbon Export) experiment, which is a contribution to the JETZON (Joint Exploration of the Twilight Zone Ocean Network) effort to assess export processes in various regions of the global ocean. During the deployment, the ocean glider was piloted to provide spatial context of mesoscale and submesoscale physical and biogeochemical tracer variability surrounding the water-mass tracking float, with a goal of attributing particle export to various carbon pump mechanisms. The existing literature on PPIPs tends to focus on a single process, *i.e.* *either* the ESP or MLP, with little previous consideration of how carbon pumps interact. We find that classification of PPIPs requires analysis of combined data sets, and consideration of tracer vertical structure, and even then can remain difficult to separate. Here, we rely on existing approaches and parameterizations to estimate PPIP magnitudes (section 3), and focus on analysis of the observational data (section 4) to offer insight in accounting for PPIPs in global estimates of the biological pump (section 5).

2 Data and Methods: a float-glider observing pair

2.1 Study region and conditions

The Southern Ocean Time Series (SOTS) observatory, established in 1997, is located at approximately 47°S, 142°E, 500 km southwest of Tasmania, Australia, in 4500 m water depth (Figure 1). SOTS is located north of a region where the Subantarctic and Polar fronts (SAF and PF) typically merge along the eastward flowing ACC. These fronts form the southern boundary of a small anticyclonic gyre, which encompasses SOTS, and is bounded to the north by subtropical waters flowing westward along the East Australian Current extension (Herraiz-Borreguero & Rintoul, 2011; Trull et al., 2001). Sediment traps moored at SOTS show a long history of hydrographic and biogeochemical properties broadly characteristic of Subantarctic waters between 90°E and 145°E (Trull et al., 2001; Shadwick et al., 2015). The proximity of the SOTS region to the SAF and PF means that this area is frequently populated by coherent mesocale eddies, which are associated with anomalies in surface temperature and chlorophyll concentrations (Figure 1a).

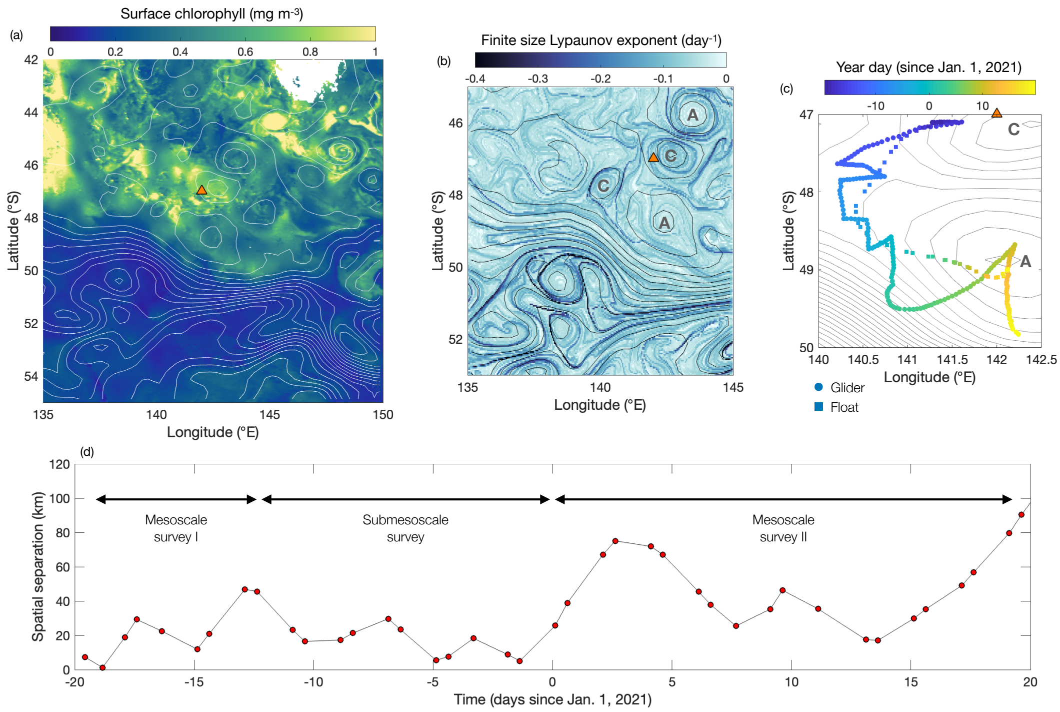

Figure 1. Overview of the SOLACE study region. (a) Snapshot of surface chlorophyll concentration (color) and sea surface height (SSH) contours (white) on December 21, 2020. (b) Satellite-derived finite size Lyapunov exponents (FSLE; section 2.4) and SSH contours (black) for December 21, 2020, highlighting regions of strong strain (negative FSLE values) at the periphery of the mesoscale eddies. The letters "A" and "C" refer to eddies with anticyclonic and cyclonic vorticity, respectively. (c) Enlarged view of SSH contours (black) and the position of the float (squares) and glider (circles), colored by year day; the SSH contours in this panel are a time average between 15 December, 2020 and 15 January, 2021. (d) Spatial separation between the float and glider (km) during the initial stage of the deployment; the sampling was divided into two longer glider mesoscale surveys and a period of shorter transects where the glider sampled within ∼20 km of the float. The time axis represents the number of days since January 1, 2021; observations from December 2020 are reported as negative days. In the upper panels, the position of the Southern Ocean Time Series (SOTS) long-term mooring is given by the orange triangle, for reference.

The SOLACE project seeks to quantify the contribution of both physically- and biologically-mediated particle injection pumps to the total export of carbon. The project combines ship-based, autonomous, and remote sensing observations. Here, we focus on data collected from two autonomous platforms, a quasi-Lagrangian float equipped with a Underwater Vision Profiler 6 (UVP6; WMO 5906623) and a Seaglider (SG674). These platforms were deployed on December 12, 2020 at 47.1°S, 141.3°E from the *R/V* Investigator. Altimetry-derived sea surface height (SSH, section 2.4) indicates that in mid-to-late December the SOLACE study region contained two cyclonic circulation features, centered at 47.8°S, 140.3°E and 47.0°S, 143.0°E and an anticyclonic circulation feature, centered at 48.8°S, 142.0°E. These cyclonic and anticyclonic eddies were associated with positive and negative surface chlorophyll anomalies, respectively (Figure 1a). The float and glider sampled in and around these eddies while remaining north of the ACC's SAF. The float's trajectory largely followed the geostrophic circulation inferred from the SSH contours. Following deployment, the float drifted to the southwest for a period of ∼2.5 weeks, until reaching the northern edge of the SAF, after which it drifted eastward (Figure 1c). In early January 2021, the float drifted into the core of the southern anticyclone, where it remained relatively stationary over a period of roughly 2 weeks before drifting back towards the northern edge of the eddy. The glider closely tracked the float position until mid-January at which time the salinity sensor on the glider became fouled; we thus focus on the period between mid-December and mid-January. Over this time, the glider completed over 200 V-shaped dives to 1000 m, producing more than 400 profiles, accounting for up- and down-casts. Each dive had a duration between 3 and 5 hr and covered a horizontal distance between 2 and 4 km. During this same period, the float completed 37 profiles.

The glider was deployed to provide both mesoscale and submesoscale context around the float. The glider sampling pattern involved multiple transects spanning roughly 10 to 100 km, and where possible, aligned these transects perpendicular to the float's trajectory. The glider survey can roughly be divided into three periods: (i) a mesoscale transect that assessed the density structure of the two cyclonic eddies located in the northern extent of the study domain; (ii) a period of shorter, rapid transects that crossed the float's trajectory with near coincident occupations of the same location (typically within less than a day); (iii) a second mesoscale transect that sampled both the SAF and the southern boundary of the anticyclone. These different periods are indicated in Figure 1d, which shows the spatial separation between the glider and float during the deployment. The time associated with each platform is provided as time in number of days since January 1, 2021; observations from December 2020 are reported as negative days.

We make use of two derived properties, spice and AOU. Spice is defined as the combination of temperature and salinity that is locally orthogonal to isolines of potential density, such that spice variance is fully density compensated (Flament, 2002). AOU is defined as the difference between oxygen solubility, determined from temperature and salinity, and the measured oxygen concentration, AOU $\equiv [O_2]_{\mathrm{sat.}} - [O_2]_{\mathrm{obs.}}$ (Ito et al., 2004).

2.2 Float data and processing

The float was a CTS5 Provor float developed by Nke Instrumentation. It carried a Sea-Bird SBE41 sensor measuring conductivity, temperature and pressure, an Aanderaa Oxygen Optode, and a WET Labs ECO Triplet measuring induced chlorophyll-a and Colored Dissolved Organic Matter (CDOM)fluorescence, and the volume scattering function at 700 nm and angle of 124°S. The volume scattering function includes scattering signal from pure seawater and particulate scattering (Zhang et al., 2009; Vaillancourt et al., 2004). The scattering by seawater was calculated using a function described in Zhang et al. (2009) and subtracted from the volume scattering function. The resulting particulate volume scattering function was converted into particulate optical backscattering coefficient bbp (Bol et al., 2018; Briggs et al., 2011). Finally, following Briggs et al. (2011), a despiked backscatter data product is also produced using a using a seven-point minimum filter followed by a seven-point maximum filter to remove spikes, which often occur in profiles of optical backscatter due to aggregate material. The CTD and trajectory data were quality-controlled using the standard Argo protocol (Wong et al., 2020). Oxygen data was calibrated to the ship-based CTD cast performed less than an hour after float and glider deployment.

The float mission included pairs of day and night profiles every 2 days from 1000 m depth to the surface at noon and from 500 m at night, with a parking depth of 1000 m. Occasionally, the float profiled down to 2000 m for the calibration of sensors not used in this study. CTD and bbp data were acquired at a vertical resolution of 0.1 m and 1 m, respectively. Oxygen data were acquired at a vertical resolution ranging from 0.1 m to 10 m depending on the depth layer.

2.3 Glider data and processing

The glider carried an unpumped CTD (CT-Sail) sensor measuring conductivity (salinity), temperature, and pressure; an Aanderaa oxygen optode; and a WET Labs ECO puck that measured induced fluorescence and optical backscatter. The salinity, temperature, and dissolved oxygen measurements from the glider sensors were calibrated to ship-based hydrographic data collected at the deployment location during the SOLACE cruise. The submesoscale phase of the glider sampling, the period of rapid crossings of the float trajectory (Figure 1b), provided additional opportunities to confirm the calibration between the two sensors. These revealed no significant sensor drift in temperature, salinity or oxygen. To conserve battery power, optical measurements were collected down to 500 m with occasional dives down to 1 km to determine a background signal. Optical backscatter data on the gliders were measured at two wavelengths: 470 and 700 nm. The glider backscatter and oxygen data were processed in the same way as the relevant float data. At times throughout the deployment when the float and glider were within 5 km of the other, parameters from the two platforms were cross-checked but no further inter-calibration was deemed necessary.

In addition to using the ungridded, processed glider data, measurements from the glider were objectively mapped onto a regular grid with 10-m depth resolution along the vertical axis and 500-m distance resolution along the horizontal axis, using a Gaussian weighting function with a vertical scale of 20 m and a horizontal scale of 5000 m, *cf.* (Viglione et al., 2018). A visual comparison of the raw data to the objectively mapped data set revealed no significant biases due to this choice of resolution. The time associated with each glider position was interpolated to the horizontal distance grid.

2.4 Altimetry-derived parameters

Daily estimates of SSH relative to the geoid for the duration of the SOLACE field program were obtained from the L4-gridded satellite altimetery product provided by Copernicus Marine Services. This includes the following data products: absolute dynamic topography (ADT), sea level anomaly (SLA), total geostrophic velocity, and eddy geostrophic velocity. The latter two fields are associated with the gradients of ADT and SLA fields, respectively.

Satellite altimetry-derived surface geostrophic velocities were used to calculate the Okubo-Weiss (OW) parameter each day during December 2020 and January 2021 (Figure 2b) and to interpolate these values in time and space to the position of the float and glider (Figure 2c). The OW parameters is given by:

$$\mathrm{OW_g} \equiv s_n^2 + s_s^2 - \zeta^2, \tag{1}$$

where the subscript 'g' indicates that OW is estimated from geostrophic velocities, and terms on the right hand side refer to the normal strain $s_n = u_x - v_y$, the shear strain $u_y + v_x$, and the vertical relative vorticity $v_x - u_y$. Regions where OW>0 and OW<0 are dominated by straining or vortical motions, respectively. The altimetry data, provided on a 25-km grid but resolving structures at larger, $O(100\text{ km})$ scales, underestimates the magnitude of vorticity and strain, which is enhanced at meso- and submesoscales. Nevertheless, during the SOLACE campaign, the float broadly occupied a region dominated by straining motions, which are more conducive to frontogenesis and the generation of submesoscale surface fronts and eddies that enhance vertical velocities. The glider sampled both vorticity- and strain-dominated regions, in particular during the two mesoscale survey period (Figure 1c).

Finite-size Lyapunov exponents (FSLEs) describe the orientation and timescale of strain fields by quantifying stretching and compression (d'Ovidio et al., 2004). They are a Lagrangian diagnostic, and for a given flow field are defined as the separation growth

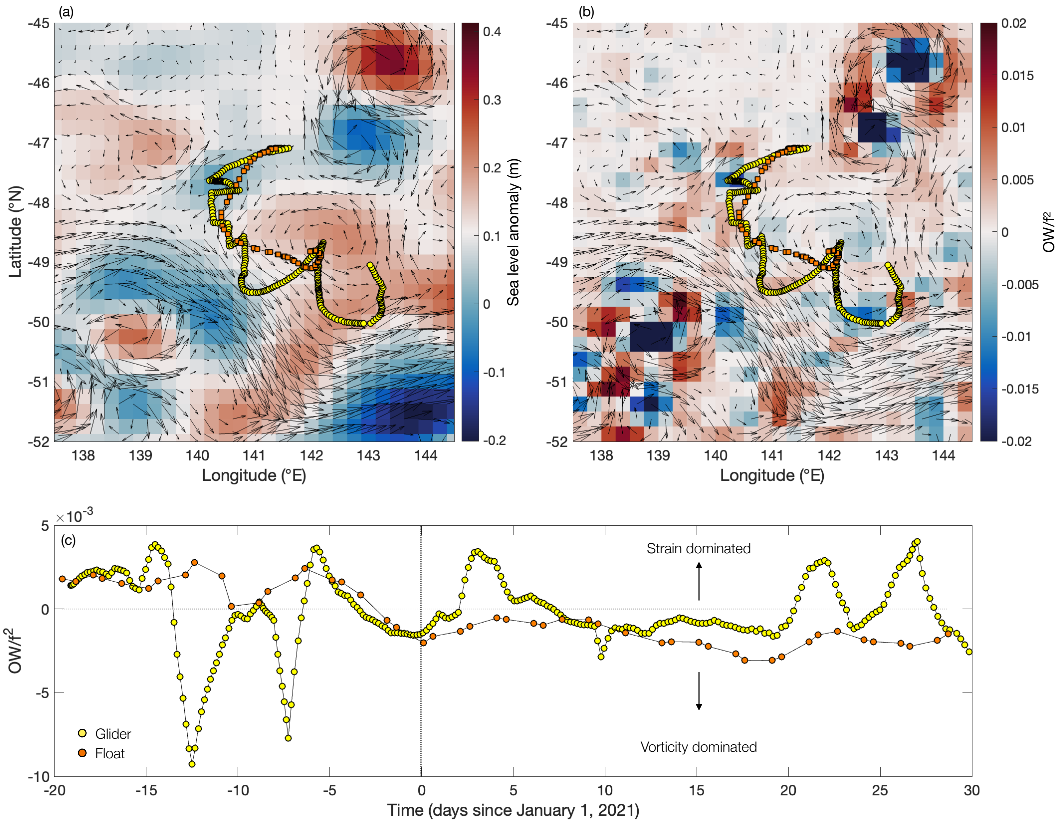

Figure 2. (a) Snapshot of the glider and float positions overlaid on sea level height anomaly (SLA, m, color) and surface geostrophic velocity (arrows) from 1 January, 2021. Coherent regions of cyclonic and anti-cyclonic vorticity are indicated by negative and positive SLA values, respectively. (b) Snapshot of the non-dimensionalized Okubo-Weiss parameteter (1) (color), where f^2 is the Coriolis frequency squared, and surface geostrophic velocity (arrows) from 1 January, 2021. Negative and positive values indicate regions dominated by vorticity and strain, respectively. (c) Time series of the OW parameter, normalized by f^2, interpolated in space and time to the position of the glider (yellow) and float (orange).

rate for seeded particle pairs. Here, FSLE estimates were computed from satellite-derived geostrophic velocities and provided by AVISO+.

Links to altimetry data products are provided in section 7.

2.5 Surface fluxes

Estimates of surface forcing fields for the region preceding, during, and after the study period were obtained from the SOTS surface mooring, which has a meteorological sensor. The data is publicly available through the Australian Ocean Data Network (AODN). Net surface heat flux was calculated as the sum of the shortwave, longwave, sensible, and latent heat flux estimates. Surface wind stress magnitude is also provided from the SOTS mooring time series. The zonal and meridional components of the wind speed, located 10 m above the surface, is calculated from the provided wind speed magnitude and the wind speed direction. The winds are predominantly westerly at the SOTS location (Figure 3b).

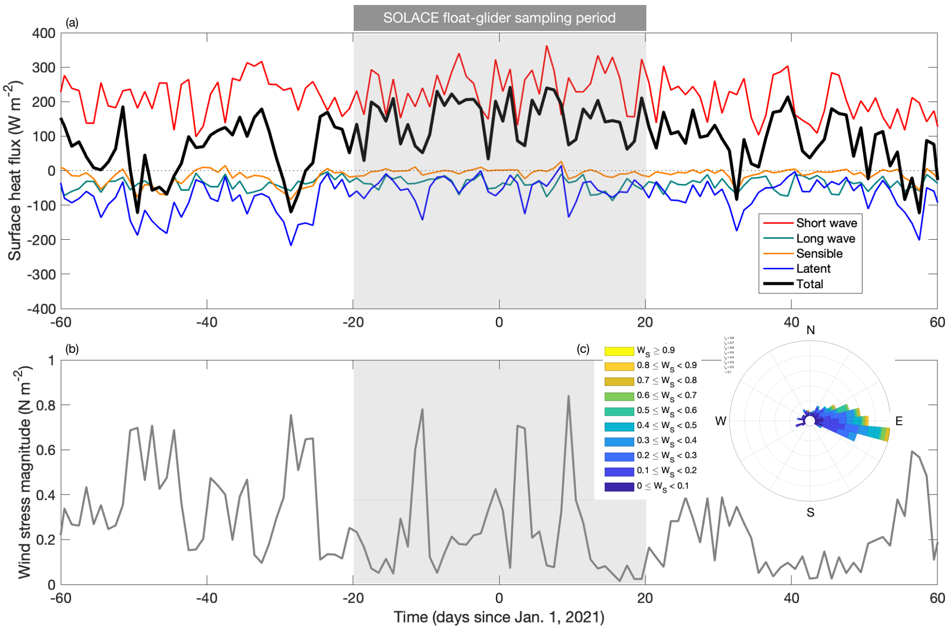

Figure 3. Surface forcing during the SOLACE field experiment as recorded at the SOTS mooring. (a) Contributions to the daily-mean ocean surface heat flux (W m^{-2}): incoming shortwave radiation (red), outgoing longwave radiaion (blue), sensible heat flux (orange), latent heat flux (green), and the total (black). (b) Wind stress magnitude derived from surface winds 10 m above the surface and (c) windrose plot showing wind speed and direction. In the windrose plot, direction shows wind speed orientation while the legend indicates wind speed magnitude.

3 Estimation of PPIPs

The main focus of this study is the time series of the ESP and the MLP as estimated from float and glider data. Ocean gliders have proven effective at resolving submesocale fronts that can be localized sites of enhanced vertical fluxes. Here, we follow the approach outlined in Omand et al. (2015) to estimate the magnitude of the ESP, noting that this formulation only accounts for motions related to mixed layer baroclinic instability. The assumption is that a relationship for the vertical export flux of POC by the ESP, $\langle w'\mathrm{POC}'\rangle$, can be linked to submesoscale upper ocean buoyancy fluxes related to near-surface restratification:

$$F_{\mathrm{ESP}} \equiv \langle w'\mathrm{POC}'\rangle \sim \langle w'b'\rangle \left\langle \frac{\partial \mathrm{POC}}{\partial z} \right\rangle \langle N^2\rangle^{-1}, \tag{2}$$

where $N^2 \equiv -g\rho_0^{-1}(\partial\sigma_0/\partial z) \approx 2\times10^{-5}$ s^{-2}. The final step connects the vertical buoyancy flux $\langle w'b'\rangle$ to a parameterized estimate of the upper ocean eddy overturning streamfunction ψ_e, such that $\langle w'b'\rangle \sim \langle -(\partial\psi_e/\partial x)\, b'\rangle \approx \psi_e M^2$. Estimating the vertical POC gradient as $[\mathrm{POC}]/h_m$, where $[\mathrm{POC}]$ is the mean mixed layer POC concentration and h_m is the MLD, gives

$$F_{\mathrm{ESP}}(t) \sim \psi_e \Gamma\, [\mathrm{POC}]\, h_m^{-1}, \tag{3}$$

where Γ is the isopycnal slope, $\Gamma = M^2/N^2$, where $M^2 \equiv g\rho_0^{-1}(\partial\sigma_0/\partial x)$, and ψ_e is estimated using the Fox-Kemper *et al.* (2008) parameterization $\psi_e = 0.08\ M^2 h_m^2 f^{-1}$. Below, M^2 is calculated from glider data with x corresponding to distance along the trajectory. The estimated F_{ESP} (3) varies quadratically with lateral density gradient M^2, and linearly with h_m and POC concentration, but varies inversely with mixed layer stratification N^2.

The export flux of carbon related to the mixed layer pump is estimated using upper ocean estimates of MLD and optical backscatter following the approach in Dall'Olmo et al. (2016) and Bol et al. (2018). To determine a time series of mixed layer POC concentration, we use the calibration presented in Schallenberg *et al.* (2016)

$$[\text{POC}] = 37{,}601 \times \text{bbp}_{700} + 4.95 \text{ mg m}^{-3}, \tag{4}$$

where bbp_{700} is the 700 nm optical backscatter value. This calibration uses observations collected during the SAZ-Sense voyage in 2007 and the SOTS voyage in 2018. The POC data from the SAZ-Sense voyage was first calibrated against the beam transmissometer, which was subsequently calibrated against bbp using data from the SOTS voyage in March 2018, when observations from both a beam transmissometer and a backscatter sensor were available on CTD casts.

Following Bol et al. (2018), we treat each observation of the mixed layer from the float and glider as part of the time series and do not explicitly account for spatial variations in the flux estimates. The limitations of this approach are discussed in section 5. The mixed layer pump is estimated by

$$F_{\text{MLP}}(t) = -\frac{1}{\Delta t}\int_{h_m(t-\Delta t)}^{h_m(t)} \overline{[\text{POC}]}(z,t)\,\mathrm{d}z, \tag{5}$$

where $\overline{[\text{POC}]}$ is the mean mixed layer POC concentration between times t and $t-\Delta t$. As defined, a reduction in the MLD ($h_m(t) < h_m(t-\Delta t)$ results in a positive export flux as POC is assumed to be left behind; as the mixed layer deepens, POC is re-entrained and $F_{\text{MLP}} < 0$. The export flux from the mixed layer pump is binned using daily, and 5-day intervals.

4 Results

4.1 Characterization of tracer variability from the float and glider

The combination of float- and glider-based measurements offers regional perspectives on mixed layer-interior exchange that are both approximately Lagrangian (float) and Eulerian (glider). The ∼daily updates of the float position enabled tight sampling between the float and glider, with the latter providing spatial context around the float and resolution of physical processes with higher temporal scales.

Differences in the float and glider tracer variability arise from two aspects of the sampling: (i) the glider resolves variations over shorter spatial and temporal scales and (ii) the float is largely sampling in a Lagrangian framework. Throughout the upper 500 m, the glider data exhibits greater tracer variability on pressure surfaces (Figure 4). Much of the physical variability is compensated, with large variations in temperature and salinity that is not expressed in density. These variations occur over characteristic scales of O(1 day, 10 km), consistent with filamentary, submesocale anomalies and are therefore not resolved by the float. The glider reveals the sharp nature of these features. For instance, a positive temperature anomaly extending to 400 m depth, that occurs at day -16 (Figure 4a,b) is recorded by both platforms, but is resolved over multiple dives in the glider. The glider also samples mesoscale anomalies in temperature and salinity linked to large vertical displacements in density surfaces (*e.g.*, day -15 to -13 and 0 to 5). These features are associated with the glider crossing coherent mesoscale eddies and the SAF. The temporal evolution of MLD is broadly similar in the float and glider (black curves in Figure 4e,f). MLD derived from the glider varies on time scales shorter than the float sampling period, which may arise from both submesoscale processes that intermittently cause the mixed layer to shoal or deepen (Thompson et al., 2016; Nicholson et al., 2022),

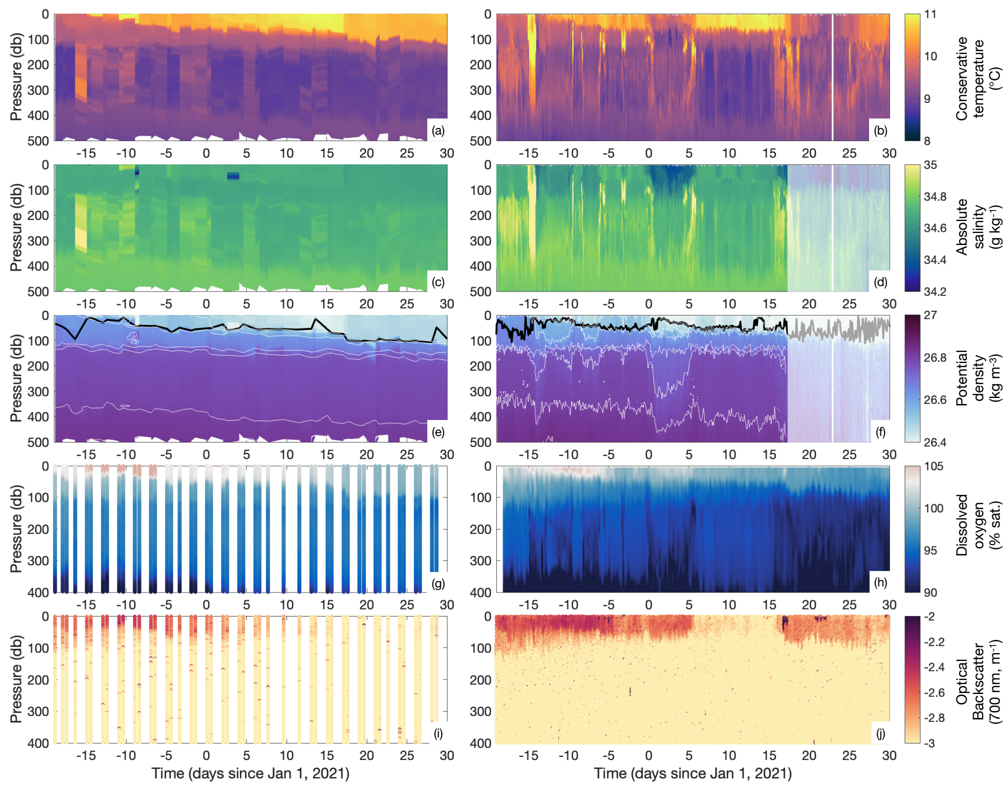

Figure 4. Hydrographic and biogeochemical properties along the trajectory of the float (left) and glider (right). The panels show (a,b) conservative temperature (°C), (c,d) absolute salinity (g kg^{-1}), (e,f) potential density σ_0 (kg m^{-3}), (g,h) dissolved oxygen (% saturation), and (i,j) $\log_{10}$ of 700 nm optical backscatter (m^{-1}). The solid black line in panels (e,f) show the mixed layer depth and white contours show density surfaces 26.5, 26.6, 26.7 26.75, 26.8, 26.85, 26.9 and 26.95 kg m^{-3}. The high frequency noise that occurs from days 18-30 in (d) and (f) are due to a fouling of the salinity sensor; these data are not considered further. The different plotting style in panels (g) and (i) is to indicate that, on the float, the biogeochemical properties are sampled at a lower vertical resolution than the physical properties.

but may also reflect spatial variability in MLD at scales less than 10 km. The glider's sampling of small-scale spatial variability in hydrographic properties provides support that the float's trajectory sampled a distinct water mass during the first month of deployment, despite its vertical profiling and the potential for vertical shear in the water column.

The distribution of temperature and salinity properties are also more compact in the float, as compared to the glider (Figure 5). Differences between Θ-S_A properties between the float and glider largely occur in the upper ocean, in density layers, $\sigma_0 < 26.7$ kg m^{-3}. The float records a near-surface layer, roughly the upper 100 m, where salinity values are uniform and stratification is dominated by temperature; this overlays a second layer, 100-400 m, with compensated temperature-salinity variations; the base of this layer is associated with the wintertime mixed layer depth (Rintoul & Trull, 2001). Deeper density classes $\sigma_0 > 26.8$ kg m^{-3} have similar distributions between float and glider and become progressively colder and fresher with depth, reaching down into AAIW water properties (Trull et al., 2001). The glider samples a broader range of near-surface salinity val-

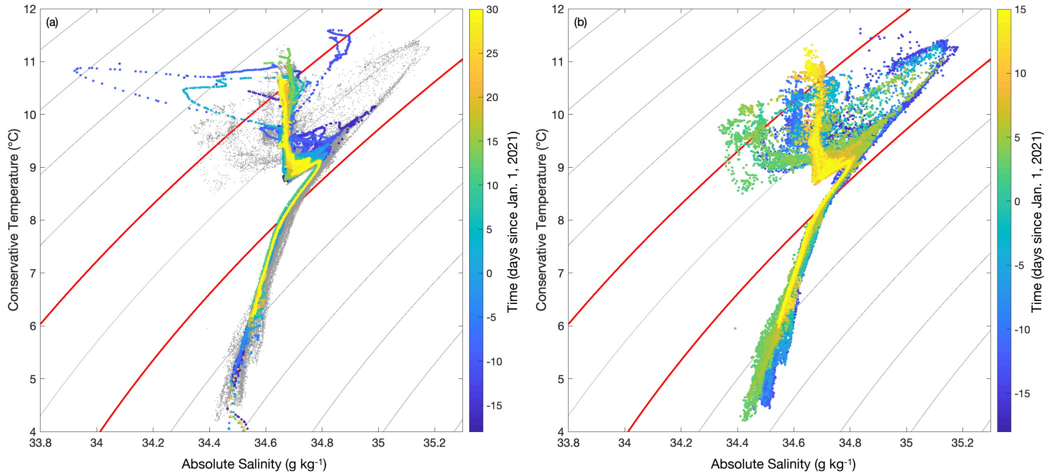

Figure 5. Distribution of conservative temperature Θ and absolute salinity S_A from the float and the glider. (a) Θ/S_A distribution from the float (colors) and glider (gray). (b) Θ/S_A distribution from the glider. Color in all panels indicates the time of the measurements given as days since January 1, 2021; note that the colorscales in the panels differ. The contours in each panel show isolines of constant potential density, σ_0, with a contour interval of 0.2 kg m^{-3}; the 26.6 and 27.0 kg m^{-3} contours are indicated by the red curves.

ues, with the coldest and freshest surface waters associated with the northern boundary of the SAF. The warmest and most saline waters are found a couple of hundred meters below the surface in the Θ-S_A compensated layer, associated with a southward flowing subsurface filaments of warm, salty subtropical waters; the strongest of these coincides with a filament between the northern anticyclone and western cyclone.

Variations in surface properties are correlated with the structure of the mesoscale flow field during the sampling period. In particular, mixed layer-averaged temperature and optical backscatter are elevated along the periphery of the coherent mesoscale features (Figure 6). These regions are also associated with the enhanced variability in MLD. The filament of warm and salty subtropical waters is collocated with an abrupt shoaling in the surface MLD as the float/glider enter region of high strain between the cyclones. These cyclones have relatively cold interior waters, and therefore the mesoscale surface tracer gradients may allow for a cascade of tracer variance to smaller scales under mesoscale and submesoscale stirring. The mixed layer-integrated backscatter values have higher variability in the glider data. Peak backscatter values coincide with the timing of the spring bloom (day -10 to -5, Figure 4) as well as during the submesoscale sampling period. The glider survey reveals $O(10)$ km-scale fronts in backscatter that are not apparent in the float data. The northern edge of the SAF and the large southern anticyclone have low backscatter values. Some of these variations might reflect the temporal evolution of the bloom, but the small scale variability observed during the glider's submesoscale survey likely reflects stirring of large scale surface variations by the mesoscale eddies (Lévy et al., 2018). These mesoscale eddies evolve over the month-long study period considered here, but the temporally averaged SSH contours shown in Figure 6 provide a reliable map of eddy cores and straining regions at the eddy edges.

Interior hydrographic and biogeochemical distributions also differ between the straining region and the latter part of the deployment when submesoscale variability is weaker (Figure 7). During the submesoscale survey, isopycals experience greater vertical displacements and there are large anomalies in spice and AOU tracers over scales of 10 km or

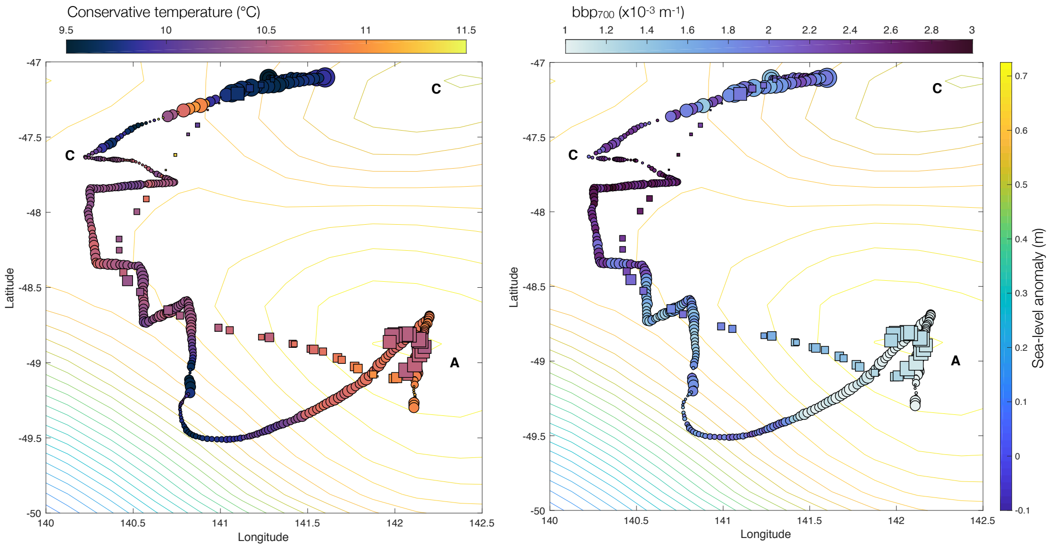

Figure 6. Surface mixed layer properties from the float and glider. (a) Mixed layer conservative temperature (°C) overlaid on sea surface height contours (m), averaged between 15 December, 2020 and 15 January, 2021. The magnitude of the symbol is linearly proportional to the mixed layer depth. Labels A and C indicate the position of coherent anti-cyclones and cyclones. (b) As in panel (a) for for mixed layer averaged 700 nm optical backscatter (m^{-1}).

less (Figure 7,d-g), where AOU anomalies also remove a mean vertical AOU profile averaged over the submesoscale section (panels f,g). Notably, spice and AOU anomalies are largely uniform throughout the upper 400 m. The horizontal scales of variability suggest the potential for generating submesoscale instabilities, but the extension below the surface boundary layer implies the importance of mesoscale motions in generating these features. The second float-glider crossing (Figure 7e,g,i) indicates that within the core of the mesoscale eddies, there is less small-scale variability and gravitational sinking likely dominates the export flux in this region. Other float-glider crossings during the submesoscale survey show similar small-scale variability to Glider Section I in Figure 7; we return to the relationship between isopycnal variations in spice/AOU and backscatter distributions in section 5.1.

The vertical stratification, as measured by the glider, shows a complex pattern of layering as a deeper (∼100-m) mixed layer restratifies in late December and early January (Figure 8a). A persistent local maximum in buoyancy frequency, N^2, is found at a depth of around 150 m. This depth is shallower than the 400-m wintertime mixed layer described by Rintoul and Trull (2001) (Figure 8b), but may represent mixed-layer deepening that occurs due to surface wind forcing. Early in the deployment, the upper ocean is weakly stratified and the MLD exceeds 100 m. Around yearday -12, the MLD shoals from greater than 100 m to $<$ 20 m. This event is associated with a reduction in the magnitude of the latent heat flux that follows the passage of a strong synoptic wind event when the wind stress approached 0.8 N m^{-2} (Figure 3). The MLD shoaling is observed at the edge of the western coherent cyclonic eddy in a region of strong surface and subsurface lateral density gradients (Figure 8c). Over the next two weeks, MLD monotonically increased, despite a positive surface heat flux, until it reached a depth of roughly 70 m. Throughout the deployment, this shallow pycnocline is separated from the deeper permanent pycnocline by a layer of low stratification, a common feature in the Southern Ocean (du Plessis et al., 2019; Siegelman et al., 2020). During January, the MLD stabilized, but N^2 at the base of the mixed layer strengthened. During the brief period

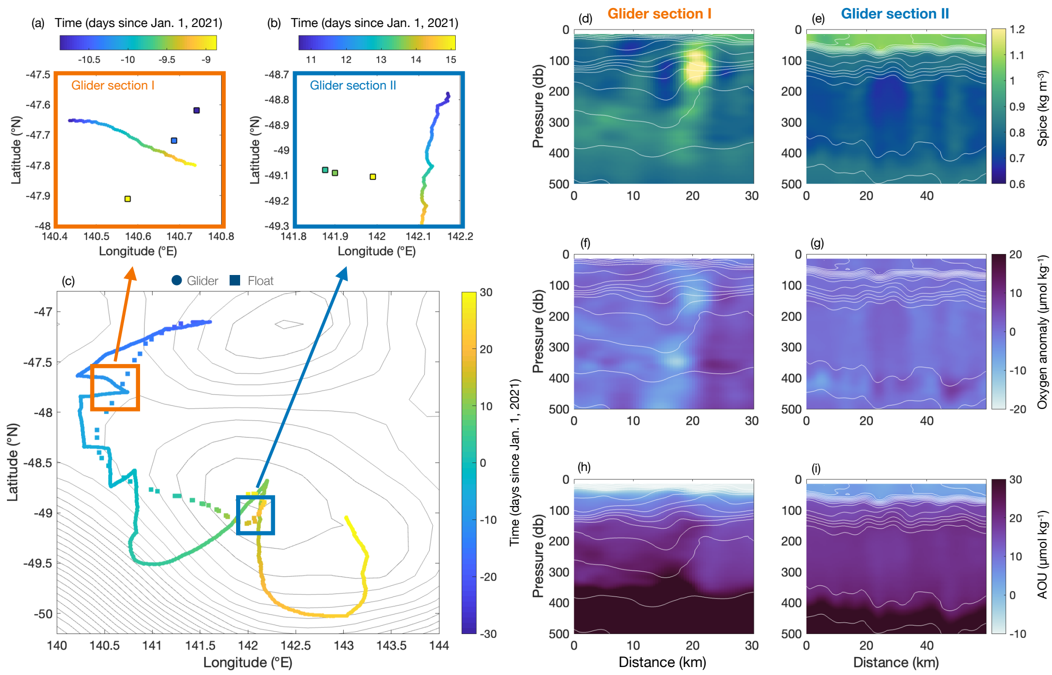

Figure 7. Submesoscale glider sections at float-glider crossovers. (a,b) Glider (circles) and float (squares) positions, colored by days since Jan. 1, 2021, at regions where they sampled in both spatial and temporal proximity. Glider section I (a) and section II (b) correspond to regions of dominant strain and vorticity, respectively (c); multiple crossovers occur in the higher strain region, as shown in panel (c). The contours in panel (c) are SSH anomaly as in Figure 1c. (d,e) Spice (kg m^3), (f,g) dissolved oxygen anomaly (μmol kg^{-3}), and (h,i) apparent oxygen utilization (AOU, μmol kg^{-3}) for Glider section I (left panels) and II (right panels). The oxygen anomaly is determined by removing the mean value at each depth over the submesocale section. The white contours in each panel indicate isopycnals with a 0.03 kg m^{-3} interval.

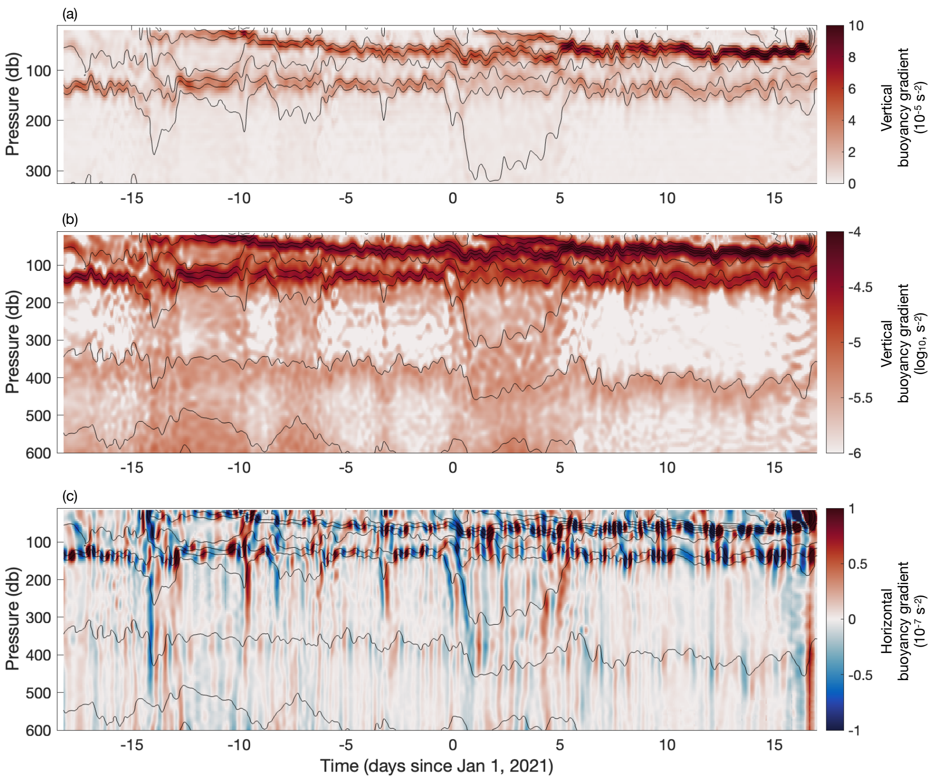

Figure 8. (a,b) Vertical stratification N^2 (defined in section 3) from the glider; note that panels (a) and (b) have different depth ranges (y-axis) and colorbars. (c) Lateral stratification M^2 (defined in section 3), along the the trajectory of the glider. In all panels, the thin gray contours are isopycnals with a 0.05 kg m^{-3} contour interval.

when the glider sampled into the SAF, there are periods when three local maxima in N^2 are found in a single vertical profile, potentially associated with the presence of submesocale coherent vortices, or SCVs, subducting from the surface boundary layer. A layer of relatively weak stratification is also found between 150 and 400 m (Figure 8b), although the magnitude of the stratification in this layer is modulated by the ocean mesoscale, with regions of enhanced stratification associated with cyclonic vorticity.

Lateral density gradients, or M^2, are dominated by oscillating positive and negative anomalies localized at the seasonal and permanent pycnoclines — the signature of internal waves (Figure 8). These oscillations are weaker in the weakly stratified region between these layers. However, deeper and vertically-coherent signature in M^2 mark the edge of mesoscale eddies in the study region. These deep fronts are consistent with other Southern Ocean observations, *e.g.* from gliders and seals, (Viglione et al., 2018; Siegelman et al., 2020), but notably occur in the SOLACE region, which is characterized by weaker EKE. Siegelman et al. (2020) argued that these deep lateral density gradients can support strong vertical velocities that extend to depths below the surface mixed layer.

4.2 Estimate of the mixed layer pump

The high-frequency sampling of the glider, roughly 10 vertical profiles per day, reveals substantial variability in MLD, including changes of up to 50 m in one day during the first week of the deployment. Daily fluctuations in MLD are damped following the onset of the seasonal pycnocline in late December, but the mixed layer continues to vary by many tens of meters on timescales of a few days to a week (Figure 9a). The float, sampling roughly once per day, captures a similar temporal evolution as the MLD (Figure 10a); due to the quasi-Lagrangian nature of the float, these variations likely record the upper ocean's response to atmospheric forcing (Figure 3). Variance in glider-derived MLD is elevated both when the mixed layer is deeper and in regions of mesoscale strain, conditions that are conducive to stronger submesoscale motions (Klein & Lapeyre, 2009). Both platforms record rapid shoaling events between yearday -17 and -15, although MLD deepens again to almost 100 m in the float time series. A longer estimate of the MLP export flux from the float has strong fluctuations in observed MLD in February and March 2021, which is also associated with the float sampling along the periphery of a coherent cyclonic mesoscale eddy (not shown).

To estimate carbon export associated with the MLP, optical backscatter data from the float and the glider are converted to a POC concentration, and then vertically averaged and vertically integrated over the depth of the mixed layer for each profile (Figure 9b and 10b). The mixed layer POC concentration gradually increases from day -20 to day -10, peaking at $\sim$ 120 mg m^{-3} during the spring bloom. From late December through January, the mixed layer POC concentration declines from 120 mg m^{-3} to 30 mg m^{-3}. The ML-integrated POC, on the other hand, exhibits finer temporal variations, reflecting fluctuations in MLD. The ML-integrated POC maximum occurs around day -17, earlier than the peak of the spring bloom, due to the deeper MLD. The differing behavior between mixed layer POC (increasing) and ML-integrated POC (decreasing) in mid-December suggests an important role for the mixed-layer pump on relatively short time scales.

Following Bol et al. (2018), daily and 5-day mean estimates of the MLP are calculated to produce a time series with a comparable temporal resolution to Bol's year-long study from the North Atlantic (Figure 9c,d). Daily estimates of carbon export have a peak magnitude of over 2-4 g POC m^{-2} and fluctuate between export (positive) and entrainment (negative) events. Averaging over a longer, 5-day, period, the daily export rates are smaller, with sustained periods of export/entrainment spanning one to two weeks, consistent with the MLD evolution recorded by the float. A sustained export event in mid-December, integrated over a 5-day period, reaches 2.25 g POC m^{-2}, although much of this export is counterbalanced by entrainment as the mixed layer deepens in late December. Between yearday -20 and 15, the daily and 5-day glider estimates produce mean carbon export rates of -90.7 and -39.2 mg POC m^{-2} day^{-1}, respectively. Patterns of carbon export and entrainment are broadly similar between the float and glider, which is expected since the glider was designed to sample water around the float (Figure 9, 10). Entrained and detrained POC concentrations were lower than the averaged mixed-layer POC concentrations, as was found by (Bol et al., 2018) (not shown), since POC concentrations decrease with depth. The amplitude of MLP fluctuations is largest at the start of the deployment when the mixed layers are deepest and surface POC concentrations are high. The effectiveness of the MLP was influenced by the fact that peak surface POC concentrations occur after MLD shoals from its deepest values (Erickson & Thompson, 2018). The timing of these two events differ by a week and would not be resolved by the typical 10-day Argo float sampling (Lacour et al., 2023).

4.3 Estimates of the eddy subduction pump

The generation of mixed layer density fronts has been identified as a potential mechanism to enhance upper-ocean vertical velocities that can advect POC out of the surface boundary layer and into the ocean interior (Omand et al., 2015). The process most widely cited for generating these vertical motions is mixed layer baroclinic instability (Boccaletti et al., 2007), in which the formation of submesoscale eddies act to restratify, or "overturn," mesoscale density fronts. This overturning gives rise to both upward and down-

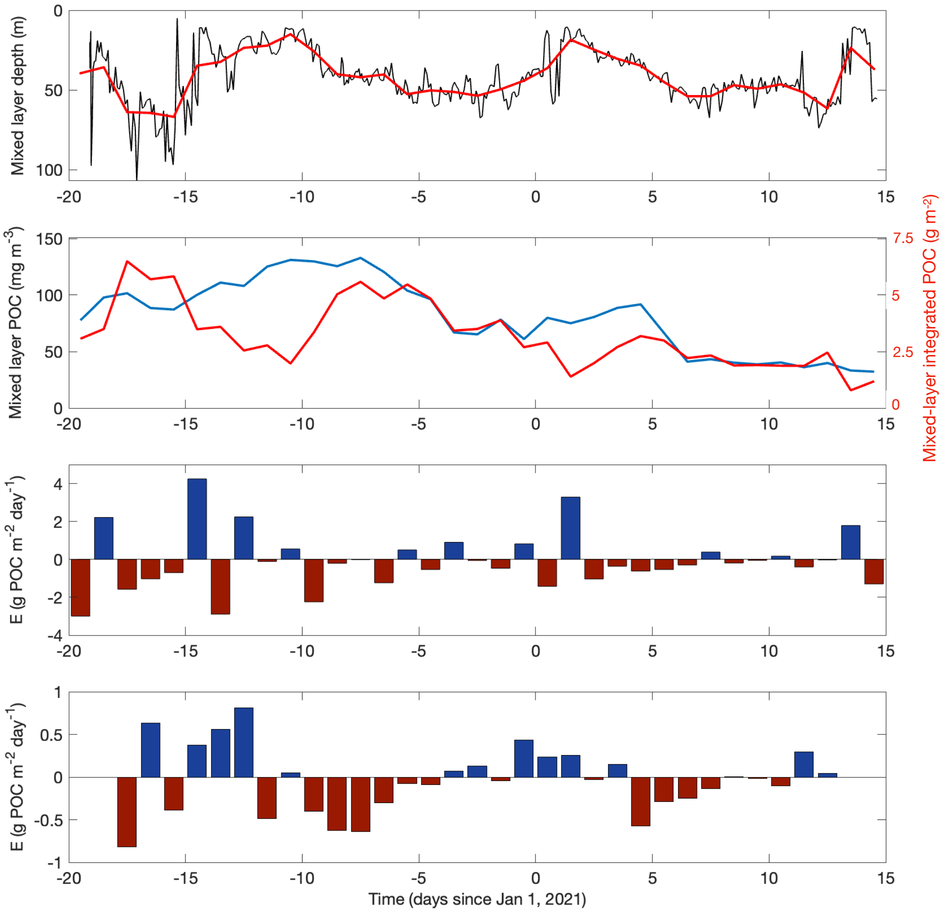

Figure 9. High-frequency mixed layer pump estimate. (a) Time series of mixed layer depth from each glider profile (black) and the glider daily-mean value (red). (b) Time series of mixed layer POC concentration (blue curve, mg m^{-3}) and POC concentration integrated over the depth of the mixed layer (red curve, g m^{-2}. (c) Daily-averaged estimate of the mixed layer pump E (g POC m^{-2} day^{-1}) as defined in equation (5) in section 3. (d) Five-day-averaged estimate of the mixed layer pump E (g POC m^{-2} day^{-1}) as defined in equation (5). In panels (c) and (d), positive and negative values are associated with POC export from and entrainment into the mixed layer, respectively.

ward motions, on the lighter and denser sides of the fronts respectively (Fox-Kemper et al., 2008; Taylor & Thompson, 2023), but supports a net downward flux of POC, assuming POC concentration decreases with depth. The scaling for the eddy subduction carbon flux in equation (3) does not explicitly resolve upwelling and downwelling components, although both observations and models provide evidence that downward POC and chlorophyll fluxes are enhanced on the dense side of fronts (Freilich & Mahadevan, 2021). We apply the scaling here with a focus on spatial variations in the magnitude of the ESP.

During the month-long deployment, variations in upper ocean stratification, both N^2 and M^2, make the dominant contribution to the temporal variability in the estimated F_{ESP} (Figure 11). As discussed above, the mixed layer undergoes a rapid shoaling event around day -17, but subsequent MLD variability is more muted (Figure 11a). Mixed layer baroclinic instability is an adiabatic process, with particles assumed to be advected along isopycnals. Thus, an increase in the tilt of density surfaces, where the isopycnal slope

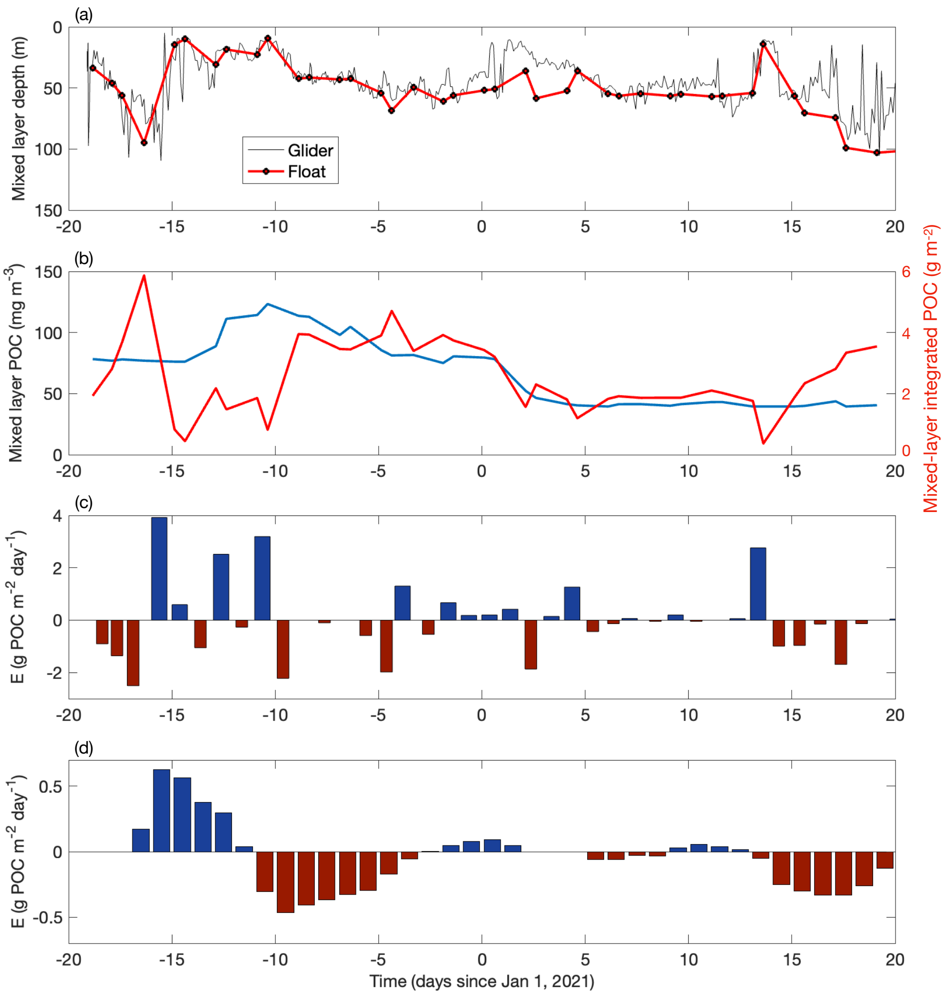

Figure 10. As in Figure 9, but for the float.

is given by the ratio M^2/N^2, are more conducive to export. Lateral buoyancy gradients are elevated earlier in the deployment, even during times, *e.g.* days -15 to -10, when the MLD is shallow (Figure 11c). The period of enhanced M^2 corresponds with times of peak N^2 during days -15 through -10 (Figure 3a), which may be a signature of effective restratifcation by submesocale eddies. The strong stratification at the base of the mixed layer differs substantially from typical North Atlantic wintertime and early springtime conditions where submesoscale fluxes have been suggested as being important for carbon export (Omand et al., 2015; Erickson & Thompson, 2018).

The mixed layer POC concentration, estimated from the optical backscatter measurements as described in section 3, are elevated throughout most of December, transitioning to moderate values around December 28. Around January 7, POC concentration drops rapidly to small values, consistent with the low values of surface backscatter measured by the float in the southern anticyclone (Figure 11d). Physical properties of the upper ocean are combined to estimate an eddy streamfunction that peaks early in the deployment when mixed layers are deepest. However, the export flux depends on both the overturning strength and the isopcynal slope. Thus, even as the eddy streamfunction weakens in late December, F_{ESP} remains intermittently > 500 mg m^{-2} day^{-1}, and peaks at almost 700 mg m^{-2} day^{-1}, around day -10; over the next few days, F_{ESP} re-

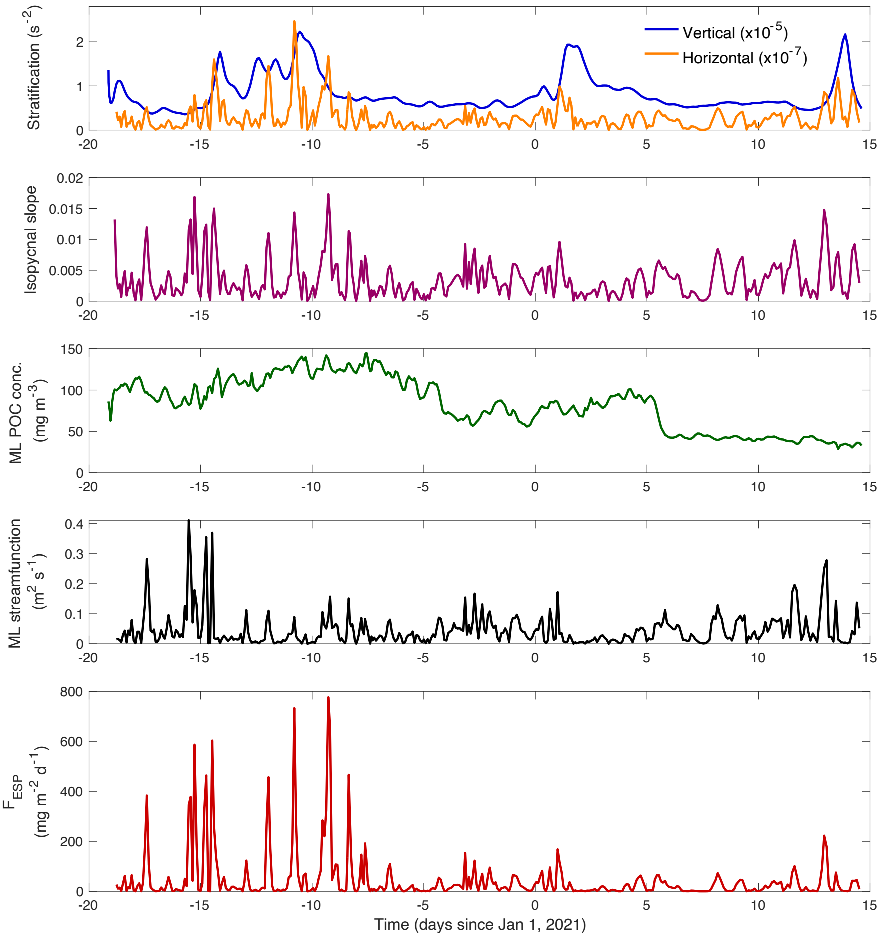

Figure 11. Estimation of the mixed layer pump along the trajectory of the glider. Time series of (a) vertical stratification, N^2 (s^{-2}), and lateral stratification M^2 (s^{-2}), integrated over the depth of the mixed layer (ML); (b) isopycnal slope, N^2/M^2; (c) POC concentration within the mixed layer (mg m^{-3}); (d) parameterized mixed layer eddy streamfunction (see discussion in section 3); and (e) time series of POC export following equation (3).

mains elevated due to a weakening N^2. This 5-day period (yearday -12 to -7) corresponds to the first part of the submesocale survey and increased variability in surface properties consistent with the presence of submesocale anomalies or stirring by submesoscale eddies. This somewhat intricate dependence of both the magnitude and phasing of multiple upper ocean properties indicates that contribution of the ESP to carbon export in any given season can be sensitive to small shifts in the surface forcing and its impact on MLD, vertical stratification, and the strength of frontogenetic and straining fields from nearby mesoscale eddies (Erickson & Thompson, 2018). Over the period, day -20 to 15, the mean value of F_{ESP} is 153 mg m^{-2} day^{-1}, and thus likely makes a stronger contribution to export than the MLP during the SOLACE field program.

5 Discussion

5.1 Isopycnal variability and the eddy subduction pump

Dynamical processes associated with coherent eddies and fronts can strongly influence biogeochemical tracer distributions and carbon export. Studies have often focused specifically on mesoscale, *e.g.*, (McGillicuddy Jr. et al., 1998; Gaube et al., 2014), or submesoscale, *e.g.* (Lévy et al., 2012; Mahadevan, 2016; Omand et al., 2015; Estapa et al., 2015; Archer et al., 2020), processes. Yet, there is growing evidence that the magnitude and variability of export fluxes depend on processes that span these scales. A rising paradigm is that mesoscale strain and stirring establish strong, near-surface lateral density gradients via frontogenesis (Balwada et al., 2018; Su et al., 2020) and enhance vertical velocities due to surface convergence (Freilich & Mahadevan, 2021). These processes give rise to ageostrophic vertical velocities that are a key component of transport across the base of the mixed layer (McWilliams, 2016; Dove et al., 2021; Taylor & Thompson, 2023). Further subduction of surface water properties in the interior is dominated by mesoscale stirring (Freilich & Mahadevan, 2021), although large submesocale vertical velocities have been inferred at depth in energetic regions of the ocean (Siegelman et al., 2020; Yu et al., 2019). Here, we examine the potential for small-scale variations in the ESP in a region of the Southern Ocean with relatively low EKE, following the paradigm outlined above.

Eddy subduction has been linked to enhanced isopycnal tracer variance of spice, an (essentially) passive tracer (Dove et al., 2021), as well as deep anomalies of low AOU waters (Llort et al., 2018). Near the SOTS region, AOU has a non-monotonic distribution when plotted against density due to interleaving between high AOU waters located to the north and relatively low AOU waters associated with AAIW (Figure 12a). This interleaving spans a vertical depth of $\sim$300 m, but is compact in density space, occurring in the range $26.8 < \sigma_0 < 26.85$ kg m^{-3}. This density layer hosts lateral gradients in AOU that are comparable to the vertical gradient in AOU (Figure 12b), varying by $\sim$40 μmol kg^{-1} over a distance of 10 km. These submesoscale anomalies in AOU are noticeably enhanced during the glider's submesoscale survey, coincident with the strongest straining region sampled by the float and glider (Figure 7). Here, anomalies are mostly vertically coherent throughout the upper 1000 m, which suggests a key role for mesoscale stirring. The anomalies are notably two to three times smaller than isopycnal AOU anomalies observed in strong stirring regions in the lee of topographic features in the ACC (Llort et al., 2018; Dove et al., 2021). The shallow sampling pattern of the float only marginally sampled the strong oxycline associated with the $\sigma_0 = 26.8$ kg m^{-3} isopycnal surface (not shown).

The distribution of spice and optical backscatter offer additional insight into the interplay between mesoscale and submesoscale features. Spice variance is dominated by relatively small-scale structures associated with straining regions found along the periphery of mesoscale eddies and fronts (Figure 13a,c). These anomalies are strongest above the the $\sigma_0 = 26.8$ kg m^{-3} isopycnal surface, but are largely found below the base of the

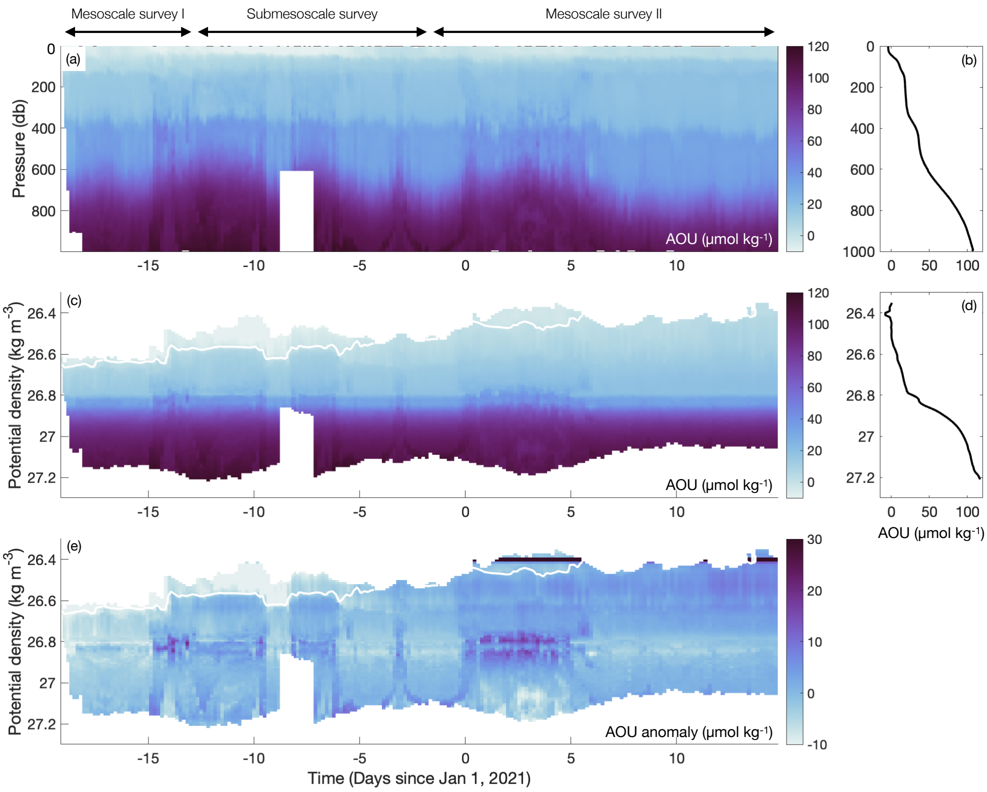

Figure 12. Apparent oxygen utilization (AOU, μmol kg^{-3}) variability along the trajectory of the glider. (a) Depth-time section of AOU, and (b) the time-mean distribution of AOU with depth covering the period shown in panel (a). (c) Density-time section of AOU, and (d) the time-mean distribution of AOU with potential density during the period shown in panel (c). (e) Density-time section of AOU anomalies, after removing the mean AOU profile shown in panel (d). The white contours in panels (c) and (e) correspond to AOU= 0 μmol kg^{-3}.

mixed layer, consistent with these features arising from mesoscale stirring, rather than submesoscale processes. Spice isolates stirring dynamics in this region, while optical backscatter integrates the effects of both advection and gravitational sinking, explaining differences in their isopycnal distributions. In depth space, backscatter has a sharp vertical gradient at the base of the mixed layer (Figure 13b), with variations across both the seasonal pycnocline and the permanent pycnocline. In density space, there is a strong vertical gradient in optical backscatter at the $\sigma_0 = 26.8$ kg m^{-3} isopycnal surface, and optical backscatter variability is particularly pronounced in the density range $26.6 < \sigma_0 < 26.8$ kg m^{-3} (Figure 13d). Elevated backscatter values occur in this density range between days -9 to -8 and days -6 to -3, for example. When considering spice and backscatter distributions together, these backscatter anomalies are bookended by the high spice values.

The optical backscatter distribution highlights the coupling between mesoscale and submesoscale dynamics on carbon export. First, periods when backscatter is elevated in the $26.6 < \sigma_0 < 26.8$ kg m^{-3} density range coincide with the displacement of isopycnals associated with coherent mesoscale cyclonic vorticity and the ACC's SAF (Figure 13a). The shoaling of the density surfaces allows this density class to be preferentially "imprinted" with sinking particles that can be efficiently stirred along density surfaces due to mesoscale stirring. As the particulate matter is advected along isopycnals, sloping density surfaces at the periphery of eddies provide pathways for enhanced carbon export that is not linked to submesocale motions, *e.g.*, $Ro = O(1)$ dynamics, but occurs at scales smaller than the coherent mesoscale eddy. A striking feature of the backscatter distribution is that a subsurface anomaly develops along the $\sigma_0 \approx 27.5$ kg m^{-3} surface, following these isopycnal shoaling events (Figure 13d-f). This injection of particulate matter along these density surfaces, in some cases, crosses into depth strata where there is a marked attenuation in particle flux in the BGP (Grabowski et al., 2019)

To estimate a subduction timescale for this process, $\tau_{\mathrm{sub.}}$, we apply a simple scaling analysis, $\tau_{\mathrm{sub.}} \sim \left(d s_\rho^{-1}\right)^2 K^{-1}$, where d is the subduction depth, K is an eddy diffusivity, and $s_\rho \equiv M^2/N^2$ is the isopycnal slope. Taking $d = 100$ m, and applying typical diffusivity values for the Southern Ocean, $K \approx 100$-1000 m^2 s^{-1}, and observed values $s_\rho \approx 0.01$ (Figure 11), subduction of POC anomalies 100 m vertically through the water column can occur over 1 to 10 days.

This mechanism, summarized in the schematic in Figure 14c, is distinct from the rapid subduction of particulate matter by enhanced submesoscale advection linked to the ESP (Ruiz et al., 2009; Llort et al., 2018). Subduction via the ESP is more consistent with the backscatter distributions found around day -13 and discussed in more detail in the next section. We note that both gravitational sinking and shallower submesoscale motions may be key for seeding certain density classes with high levels of particular matter that can be redistributed vertically and horizontally by interior mesoscale stirring.

5.2 Separating contributions from mixed layer and eddy subduction pumps

The two PPIPs considered in this study, the MLP and ESP, each have a strong dependence on MLD and upper ocean stratification. For the MLP, a reduction in MLD, originally envisioned as due to surface forcing (Gardner et al., 1995), results in a passive removal of POC from the surface boundary layer and, through subsequent sinking, an escape from future re-entrainment when the mixed layer deepens again. In contrast, the ESP mechanism involves the generation of surface density gradients that support strong vertical velocities and an active advection of POC from the surface boundary layer. The signature of export by the ESP is difficult to distinguish from sparse, often one- or two-dimensional, observations, especially when subsurface POC anomalies are displaced laterally from the location where they exited the mixed layer. Additionally, mixed layer baro-

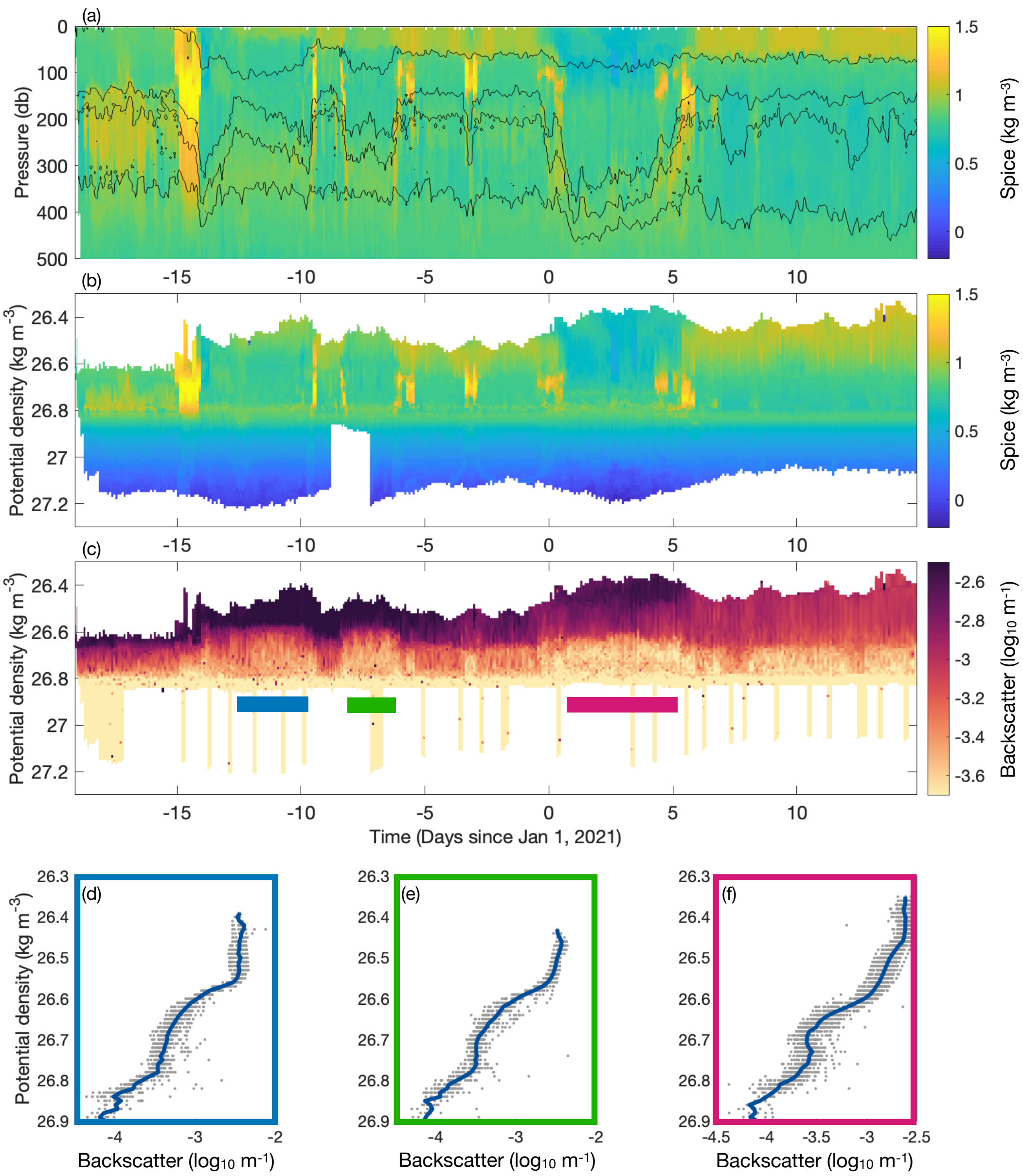

Figure 13. (a) Spice (color) and potential density, σ_0 (contours) along the glider trajectory, both with units kg m^{-3}; the σ_0 contours are 26.6, 26.76, 26.78, and 26.8 kg m^{-3}. (b) Spice and (c) optical backscatter (bbp, m^{-1}) mapped on to potential density surfaces with a 0.01 kg m^{-3} interval. Lower panels: time-averaged bbp during the year day intervals, -13 to -10 (panel d, blue), -8 to -6 (panel 3, green), and 0 to 5, (panel f, magenta).

clinic instability leads to a shoaling and restratification of the mixed layer, which can make attribution of carbon export from an individual PPIP challenging.

The first half of the SOLACE deployment highlights two distinct scenarios in which MLP and ESP pumps interact. The export flux event centered around day -15 is associated with (i) a rapid shoaling of the mixed layer, (ii) peak values of the eddy overturning streamfunction (Figure 11) and (iii) a deep-reaching density front in the high strain region between the two cyclones (Figure 1). Furthermore, in mid-December 2020 this region was characterized by a diverse phytoplankton assemblage, from small pico-eukaryotes to large diatoms, with a high photosynthetic competence (F_v/F_m), and hence cells likely had negligible sinking rates (E. Shadwick, personal communication). This suggests that injection to depth via physically-mediated injection pumps was the dominant export pathway.

As discussed in section 5.1, day -15 marks the initiation of enhanced interior tracer gradients (spice and apparent oxygen utilization), but most of the shoaling of the mixed layer happens one or two days earlier. The mixed layer shoaling follows a reduction in the surface wind stress, a reduction in the magnitude of the latent heat flux, and an increase in the total surface heat flux (Figure 3). This is consistent with carbon export in response to 1D surface forcing. Thus, during this period, any contribution to POC export from the ESP would have occurred due to the surface-forcing induced mixed-layer shoaling, or the MLP. In this scenario, it is not appropriate to sum the two PPIP contributions. We propose that the PPIP contribution is likely to be better represented by the maximum of carbon flux estimated from the MLP and ESP parameterizations (Figure 14a). For this study, the estimated contributions from the MLP and ESP are of comparable magnitude during this short period.

The ESP has two strong peaks, one occurring between days -17 to -15, associated with deep mixed layers, and the second between days -12 to -8, associated with relatively shallow mixed layers but enhanced lateral density gradients and a weakened vertical stratification N^2. In the latter period, the ESP and MLP work in opposition, with $F_{\text{ESP}} > 0$ and $F_{\text{MLP}} < 0$. Frontogenesis occurring in this straining region provides conditions that are conducive to strengthening F_{ESP}, even as the the mixed layer slowly deepens, entraining potentially subducted POC. The two PPIPs cancel to leading order, although averaging over this four day period gives a slight tendency for export (Figure 14b). The mixed layer deepening is likely a broad response to wind-driven mixing since increasing MLD is recorded in both the float and glider data, whereas subduction via the ESP is more spatially localized.

A limitation of the Omand et al. (2015) scaling is that the vertical structure of the ESP is not explicitly addressed. If the vertical advection is sufficiently deep that particulate matter escapes subsequent deepening of the mixed layer, then this export would not be offset by the MLP (Figure 14b). These interactions highlight a major challenge with defining appropriate export horizons for export flux calculations if both PPIPs are active: the MLP is best assessed in depth, relative to the depth of the mixed layer base, whereas the ESP is easier to diagnose in density space.

6 Conclusions

The SOLACE data set, as a whole, provides a unique opportunity to estimate the combined contributions from multiple particle injection pumps to carbon export in the Subantarctic Zone of the Southern Ocean. This study (i) provides contextual hydrographic and biogeochemical observations from the region due to the broad sampling of the float-glider observing pair, and (ii) conducts a first attempt to isolate contributions from two PPIPs, the MLP and ESP. While the SOTS region is a relatively low EKE region of the Southern Ocean, there is compelling evidence that physical processes spanning meso- and

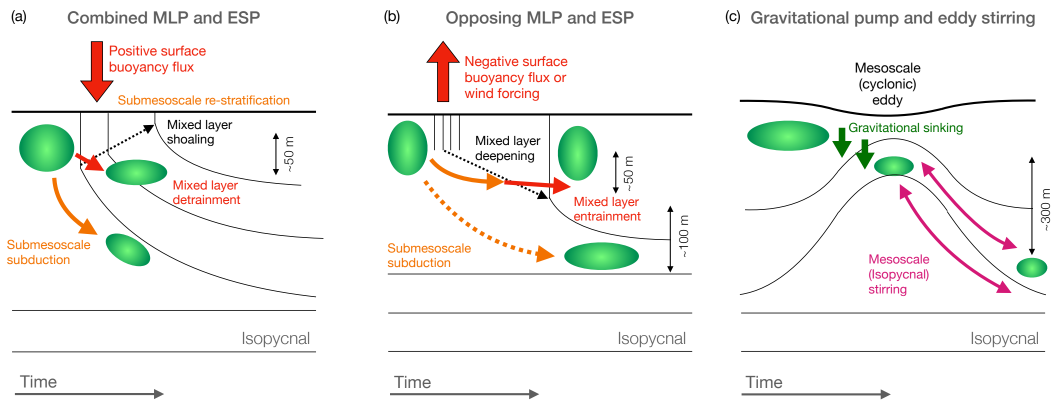

Figure 14. Examples of combined particle injection pumps. (a) Positive surface buoyancy forcing in the presence of submesoscale surface fronts can cause carbon export through both eddy subduction and detrainment (mixed layer shoaling); these processes may be difficult to separate unless subduction injects carbon to deeper depths and density classes. (b) Eddy subduction may occur during periods of entrainment (mixed layer deepening); the ESP and MLP would cancel unless subduction injects carbon to depths where it is not re-entrained. (c) Mesoscale eddies can shoal density surfaces, allowing gravitational sinking to intermittently imprint particles on the deeper density classes; subsequent along-isopycnal stirring, which is enhanced at the eddy periphery, can efficiently carry these particles to depth.

submesoscales make a significant contribution to the export of carbon following the onset of the spring bloom. The timing of mixed layer restratification coincided with the float/glider occupying a region of mesoscale strain and associated enhanced lateral density gradients, such that both the MLP and ESP were likely active and contributing to the export of the same carbon stock. This highlights some of the potential complications with simply summing carbon fluxes estimated from PPIPs in isolation.

While the primary focus of this study was on PPIPs, the interior shaping of the density surfaces by mesoscale eddies are also shown to influence the vertical transport of POC. In regions of cyclonic vorticity, density classes that are typically many hundreds of meters below the base of the mixed layer shoal by $O(100\text{ m})$ or more and are exposed to higher POC concentrations as a result of gravitational sinking. Sampling with a single glider and quasi-Lagrangian float does not permit direct tracking of these POC anomalies, but assuming typical mesoscale isopycnal stirring diffusivities, 100-1000 m^2 s^{-1} and an isopcynal slope of 0.01, vertical displacements of $\sim$100 m may occur on the order of days. This coupling between gravitational and advective fluxes will be strongest in submesoscale regions on the periphery of eddies where strain and isopycnal tilt is enhanced.

In addition to the challenge of distinguishing carbon flux contributions from various PPIPs using sparse observations, a theoretical framework for determining global and annual contributions from these PPIPs is daunting. Selecting an appropriate export horizon, or the depth below organic carbon is considered exported (Palevsky & Doney, 2018), to estimate an export flux may be sensitive to not only local mixed layer depth, but also the stratification at the base of the mixed layer, the range of densities that outcrop in the mixed layer, and the interior density structure. Future efforts should, through a combination of observational analysis and high-resolution process-based modeling, focus on improving mechanistic understanding of how the vertical structure of physical and biogeochemical properties relate to export flux magnitudes and the relevant carbon pumps.

7 Open Research

Surface flux and forcing data is available through the Australian Ocean Data Network at `https://portal.aodn.org.au/`. Sea level anomaly and surface velocity products were produced and distributed by the Copernicus Marine 360 and Environment Monitoring Service and are available at `https://data.marine.copernicus.eu/product/SEALEVEL_GLO_PHY_L4_MY_008_047/description`. Finite-size Lyapunov Exponents were produced and distributed by AVISO+ and are available at `https://www.aviso.altimetry.fr/en/data/products/value-added-products/fsle-finite-size-lyapunov-exponents.html`

Glider data presented in this work has been uploaded to the NOAA National Centers for Environmental Information (NCEI) database and is accessible at `https://www.ncei.noaa.gov/archive/accession/0276999`.

Float data can be downloaded from the Argo Global Data Assembly Center (`ftp://ftp.ifremer.fr/ifremer/argo/`). These data were collected and made freely available by the International Argo Program and the national programs that contribute to it: (`http://www.argo.ucsd.edu`, `https://www.ocean-ops.org`). The Argo Program is part of the Global Ocean Observing System.

Acknowledgments

We are grateful for the efforts of the full SOLACE field team as well as the captain and crew of the R/V Investigator. We extend particular thanks to Tyler Rohr who took on extra glider testing, deployment and troubleshooting responsibilities during the cruise due to COVID travel restrictions. The authors acknowledge helpful suggestions and conversations from Elizabeth, Shadwick, Tom Trull, Mara Freilich, and Alice Della Penna. AFT, LAD and EF were supported by the Resnick Sustainability Institute and the Ginkgo Foundation; LAD received additional support from an NSF graduate research fellowship. EF's contributions were supported by a Summer Undergraduate Research Fellowship at Caltech. LL was supported by a European Union's Horizon 2020 Marie Sklodowska-Curie grant (no. 892653).

References

Archer, M., Schaeffer, A., Keating, S., Roughan, M., Holmes, R., & Siegelman, L. (2020). Observations of submesoscale variability and frontal subduction within the mesoscale eddy field of the Tasman Sea. *J. Phys. Oceanogr.*, *50*, 1509-1529.

Balwada, D., Smith, K. S., & Abernathey, R. (2018). Submesoscale vertical velocities enhance tracer subduction in an idealized Antarctic Circumpolar Current. *Geophys. Res. Lett.*, *45*, 9790-9802.

Boccaletti, G., Ferrari, R., & Fox-Kemper, B. (2007). Mixed layer instabilities and restratification. *J. Phys. Oceanogr.*, *37*(9), 2228–2250.

Bol, R., Henson, S. A., Rumyantseva, A., & Briggs, N. (2018). High-frequency variability of small-particle carbon export flux in the northeast Atlantic. *Global Biogeochem. Cycles*, *32*, 1803-1814.

Boyd, P. W., Claustre, H., Lévy, M., Siegel, D. A., & Weber, T. (2019). Multi-faceted particle pumps drive carbon sequestration in the ocean. *Nature*, *568*, 327-335.

Brady, R. X., Maltrud, M. E., Wolfram, P. J., Drake, H. F., & Lovenduski, N. S. (2021). The disproportionate role of ocean topography on the upwelling of carbon in the Southern Ocean. *Geophys. Res. Lett.*, *48*, e2021GL095088.

Brannigan, L. (2016). Intense submesoscale upwelling in anticyclonic eddies intense submesoscale upwelling in anticyclonic eddies intense submesoscale upwelling in anticyclonic eddies. *Geophys. Res. Lett.*, *43*, 3360–3369.

Briggs, N., Perry, M. J., Cetinić, I., Lee, C., D'Asaro, E., Gray, A. M., & Rehm, E. (2011). High-resolution observations of aggregate flux during a sub-polar North Atlantic spring bloom. *Deep-Sea Res. I*, *58*, 1031-1039.

Bushinsky, S. M., Landschützer, P., Rödenbeck, C., Gray, A. R., Baker, D., Mazloff, M. R., ... Sarmiento, J. L. (2019). Reassessing Southern Ocean air-sea CO_2 flux estimates with the addition of biogeochemical float observations. *Global Biogeochem. Cycles*, *33*, 1370-1388.

Callies, J., Flierl, G., Ferrari, R., & Fox-Kemper, B. (2016). The role of mixed-layer instabilities in submesoscale turbulence. *J. Fluid Mech.*, *788*, 5-41.

Cornec, M., Laxenaire, R., Speich, S., & Claustre, H. (2021). Impact of mesoscale eddies on deep chlorophyll maxima. *Geophys. Res. Lett.*, *48*, e2021GL093470.

Dall'Olmo, G., Dingle, J., Polimene, L., Brewin, R. J. W., & Claustre, H. (2016). Substantial energy input to the mesopelagice ecosystem from the seasonal mixed-layer pump. *Nat. Geosci.*, *9*, 820-823.

Damerell, G. M., Heywood, K. J., Calvert, D., Grant, A. L. M., Bell, M. J., & Belcher, S. E. (2020). A comparison of five surface mixed layer models with a year of observations in the north atlantic. *Prog. Oceanogr.*, *187*, 102316.

Dove, L. A., Balwada, D., Thompson, A. F., & Gray, A. R. (2022). Enhanced ventilation in energetic regions of the Antarctic Circumpolar Current. *Geophys. Res. Lett.*, *49*, e2021GL097574.

Dove, L. A., Thompson, A. F., Balwada, D., & Gray, A. R. (2021). Observational evidence for ventilation hotspots in the Southern Ocean. *J. Geophys. Res. Oceans*, in review.

Dove, L. A., Viglione, G. A., Thompson, A. F., Flexas, M. M., Cason, T. R., & Sprintall, J. (2023). Controls on wintertime ventilation in southern Drake Passage. *Geophys. Res. Lett.*, in press.

d'Ovidio, F., Fernández, V., Henández-García, E., & López, C. (2004). Mixing structures in the Mediterranean Sea from finite-size Lyapunov exponents. *Geophys. Res. Lett.*, *31*, L17203.

du Plessis, M., Swart, S., Ansorge, I. J., Mahadevan, A., & Thompson, A. F. (2019). Southern Ocean seasonal restratification delayed by submesoscale wind-front interactions. *J. Phys. Oceanogr.*, *49*, 1035-1053.

Erickson, Z. K., & Thompson, A. F. (2018). The seasonality of physically driven export at submesoscales in the northeast Atlantic Ocean. *Global Biogeochem. Cycles*, *32*, 1144-1162.

Estapa, M. L., Siegel, D. A., Busseler, K. O., Stanley, R. H. R., Lomas, M. W., & Nelson, N. B. (2015). Decoupling of net community and export production on submesoscale in the Sargasso Sea. *Global Biogeochem. Cycles*, *29*.

Flament, P. (2002). A state variable for characterizing water masses and their diffusive stability: spiciness. *Prog. Oceanogr.*, *54*(493-501).

Fox-Kemper, B., Ferrari, R., & Hallberg, R. (2008, 2015/05/11). Parameterization of mixed layer eddies. part I: Theory and diagnosis. *J. Phys. Oceanogr.*, *38*, 1145–1165.

Freilich, M., & Mahadevan, A. (2021). Coherent pathways for subduction from the surface mixed layer at ocean fronts. *J. Geophys. Res. Oceans*, *126*, e2020JC017042.

Gardner, W. D., Chung, S. P., Richardson, M. J., & Walsh, I. D. (1995). The oceanic mixed layer pump. *Deep-Sea Res. II*, *42*, 757-775.

Gaube, P., McGillicuddy Jr., D. J., Chelton, D. B., Behrenfeld, M. J., & Strutton, P. G. (2014). Regional variations in the influence of mesoscale eddies on near-surface chlorophyll. *J. Geophys. Res. Oceans*, *119*, 8195–8220.

Giddy, I., Nicholson, S. A., Queste, B. Y., Thomalla, S. J., & Swart, S. (2022). Sea-ice impacts inter-annual variability in bloom phenology and carbon export. *Geophys. Res. Lett.*, submitted.

Giddy, I., Swart, S., du Plessis, M., Thompson, A. F., & Nicholson, S. A. (2021). Stirring of sea-ice meltwater enhances submesoscale fronts in the Southern Ocean. *J. Geophys. Res. Oceans*, *126*, e2020JC016814.

Gille, S. T., & Kelly, K. A. (1996). Scales of spatial and temporal variability in the Southern Ocean. *J. Geophys. Res.*, *101*, 8759-8773.

Gille, S. T., Sheen, K. L., Swart, S., & Thompson, A. F. (2022). Mixing in the Southern Ocean. In M. Meredith & A. C. Naveira Garabato (Eds.), *Ocean mixing: Drivers, mechanisms and impacts.* Cambridge University Press.

Grabowski, E., Letelier, R. M., Laws, E. A., & Karl, D. M. (2019). Coupling carbon and energy fluxes in the North Pacific Subtropical Gyre. *Nat. Comm.*, *10*, 1895.

Herraiz-Borreguero, L., & Rintoul, S. R. (2011). Regional circulation and its impact on upper ocean variability south of Tasmania. *Deep-Sea Res. II*, *58*, 2071-2081.

Ito, T., Follows, M. J., & Boyle, E. A. (2004). Is AOU a good measure of respiration in the oceans? *Geophys. Res. Lett.*, *31*, L17305.

Klein, P., & Lapeyre, G. (2009). The oceanic vertical pump induced by mesoscale and submesoscale turbulence. *Ann. Rev. Mar. Sci.*, *1*, 351–375.

Kwon, E. Y., Primeau, F., & Sarmiento, J. L. (2009). The impact of remineralization depth on the air-sea carbon balance. *Nat. Geosci.*, *2*, 630-635.

Lacour, L., Llort, J., Briggs, N., Strutton, P. G., & Boyd, P. W. (2023). Seasonality of downward carbon export in the Pacific Southern Ocean revealed by multi-year robotic observations. *Nat. Comm.*, *14*, 1278.

Lévy, M., Ferrari, R., Franks, P. J. S., Martin, A. P., & Rivière, P. (2012). Bringing physics to life at the submesoscales. *Geophys. Res. Lett.*, *39*, L14602.

Lévy, M., Franks, P. J. S., & Smith, K. S. (2018). The role of submesoscale currents in structuring marine ecosystems. *Nat. Comm.*, *9*, 4758.

Llort, J., Langlais, C., Matear, R., Moreau, S., Lenton, A., & Strutton, P. G. (2018). Evaluating Southern Ocean carbon eddy-pump from Biogeochemical-Argo floats. *J. Geophys. Res. Oceans*, *123*, 971-984.

Mahadevan, A. (2016). The impact of submesoscale physics on primary productivity of plankton. *Ann. Rev. Fluid Mech.*, *8*, 17.1–17.24.

McGillicuddy Jr., D. J., Robinson, A. R., Siegel, D. A., Jannasch, H. W., Johnson, R., adn J. McNeil, T. D. D., … Knap, A. H. (1998). Influence of mesoscale eddies on new production in the Sargasso Sea. *Nature*, *394*, 263-266.

McWilliams, J. C. (2016). Submesoscale currents in the ocean. *Proc. R.. Soc. A*, *472*, 20160117.

Nicholson, S.-A., Whitt, D. B., Fer, I., duPlessis, M. D., Lebéhot, A. D., Swart, S., … Monteiro, P. M. S. (2022). Storms drive outgassing of co_2 in the subpolar Southern Ocean. *Nat. Comm.*, *13*, 158.

Omand, M. M., D'Asaro, E. A., Lee, C. M., Perry, M. J., Briggs, N., Cetini, I., & Mahadevan, A. (2015). Eddy-driven subduction exports particulate organic carbon from the spring bloom. *Science*, *348*, 222–223.

Palevsky, H. I., & Doney, S. C. (2018). How choice of depth horizon influences the estimated spatial patterns and global magnitude of ocean carbon flux export. *Geophys. Res. Lett.*, *45*, 4171-4179.

Patel, R. S., Llort, J., Strutton, P. G., Phillips, H. E., Moreau, S., Conde Pardo, P., & Lenton, A. (2020). The biogeochemical structure of Southern Ocean mesoscale eddies. *J. Geophys. Res. Oceans*, *125*, e2020JC016115.

Penna, A. D., Llort, J., Moreau, S., Patel, R., Kloser, R., Gaube, P., … Boyd, P. W. (2022). The impact of a Southern Ocean cyclonic eddy on msopelagic micronekton. *J. Geophys. Res. Oceans*, *127*, e2022JC018893.

Rintoul, S. R., & Trull, T. W. (2001). Seasonal evolution of the mixed layer in the Subantarctic Zone south of Australia. *J. Geophys. Res.*, *106*, 31,447-31,462.

Rohr, T., Harrison, C., Long, M. C., Gaube, P., & Doney, S. C. (2020a). Eddymodified iron, light, and phytoplankton cell division rates in the simulated southern ocean. *Global Biogeochem. Cycles*, *34*, e2019GB006380.

Rohr, T., Harrison, C., Long, M. C., Gaube, P., & Doney, S. C. (2020b). The simulated biological response to Southern Ocean eddies via biological rate modification and physical transport. *Global Biogeochem. Cycles*, *34*, e2019GB006385.

Ruiz, S., Claret, M., Pascual, A., Olita, A., Troupin, C., Capet, A., . . . Mahadevan, A. (2019). Effects of oceanic mesoscale and submesoscale frontal processes on vertical transport of phytoplankton. *J. Geophys. Res. Oceans*, *124*(5999-6014).

Ruiz, S., Pascual, A., Garau, B., Pujol, I., & Tintoré, J. (2009). Vertical motion in the upper ocean from glider and altimetry data. *Geophys. Res. Lett.*, *36*, L14607.

Sarmiento, J. L., & Gruber, N. (2006). *Ocean Biogeochemical Dynamics*. Princeton University Press.

Shadwick, E. H., Trull, T. W., Tillbrook, B., Sutton, A. J., Schulz, E., & Sabine, C. L. (2015). Seasonality of biological and physical controls of surface ocean co_2 from hourly observations at the Southern Ocean Time Series site south of Australia. *Global Biogeochem. Cycles*, *29*, 2014GB004906.

Siegel, D. A., DeVries, T., Cetinić, I., & Bisson, K. M. (2023). Quantifying the ocean's biological pump and its carbon cycle impacts on global scales. *Ann. Rev. Mar. Sci.*, *15*, 18.1-18.28.

Siegelman, L., Klein, P., Rivière, P., Thompson, A. F., Torres, H. S., Flexas, M., & Menemenlis, D. (2020). Enhanced upward heat transport at deep submesoscale ocean fronts. *Nat. Geosci.*, *13*, 50-55.

Stukel, M. R., & Ducklow, H. W. (2017). Stirring up the biological pump: vertical mixing and carbon export in the Southern Ocean. *Global Biogeochem. Cycles*, *31*, 1420-1434.

Su, Z., Torres, H., Klein, P., Thompson, A. F., Siegelman, L., Wang, J., . . . Hill, C. (2020). High-frequency submesoscale motions enhance the upward vertical heat transport in the global ocean. *J. Geophys. Res. Oceans*, *125*, e2020JC016544.

Taylor, J. R. (2018). Accummulation and subduction of buoyant material at submesoscale fronts. *J. Phys. Oceanogr.*, *48*, 1233-1241.

Taylor, J. R., & Thompson, A. F. (2023). Submesoscale dynamics in the upper ocean. *Ann. Rev. Fluid Mech.*, *55*, 103-127.

Thomas, L. N., Taylor, J. R., Ferrari, R., & Joyce, T. M. (2013). Symmetric instability in the Gulf Stream. *Deep Sea Res. II*, *91*, 96–110.

Thompson, A. F., Lazar, A., Buckingham, C., Garabato, A. C. N., Damerell, G. M., & Heywood, K. J. (2016). Open-ocean submesoscale motions: A full seasonal cycle of mixed layer instabilities from gliders. *J. Phys. Oceanogr.*, *46*, 1285–1307.

Trull, T. W., Bray, S. G., Manganini, S. J., Honjo, S., & François, R. (2001). Moored sediment trap measurements of carbon export in the Subantarctic and Polar Frontal zones of the Southern Ocean, south of Australia. *J. Geophys. Res.*, *106*, 31489-31509.

Vaillancourt, R. D., Brown, C. W., Guillard, R. R. L., & Balch, W. M. (2004). Ligh backscattering properties of marine phytoplankton: Relationships to cell size, chmical composition and taxonomy. *J. Plankton Res.*, *26*, 191-212.

Viglione, G. A., Thompson, A. F., Flexas, M. M., Sprintall, J., & Swart, S. (2018). Abrupt transitions in submesoscale structure in southen Drake Passage: Glider observations and model results. *J. Phys. Oceanogr.*, *48*, 2011-2027.

Wong, A., Keeley, R., Carval, T., & Argo Data Management Team. (2020). Arog quality control manual for CTD and trajectory data [Computer software manual].

Yamanaka, Y., & Tajika, E. (1996). The role of the vertical fluxes of particular organic matter and calcite in the ocean carbon cycle: Studies using an ocean biogeochemical general circulation model. *Global Biogeochem. Cycles*, *10*, 361-382.

Yu, X., Naveira Garabato, A. C., Martin, A. P., Buckingham, C. E., Brannigan, L., & Su, Z. (2019). An annual cycle of submesoscale vertical flow and restratification in the upper ocean. *J. Phys. Oceanogr.*, *49*, 1439-1461.

Zhang, X., Hu, L., & He, M.-X. (2009). Scattering by pure seawater: Effect of salinity. *Optics Express*, *17*, 5698-5710.